

Cerebral oxygen extraction fraction MRI: techniques and applications

Dengrong Jiang¹, Hanzhang Lu^{1,2,3}

¹The Russell H. Morgan Department of Radiology & Radiological Science, Johns Hopkins University School of Medicine, Baltimore, Maryland, USA.

²Department of Biomedical Engineering, Johns Hopkins University School of Medicine, Baltimore, Maryland, USA.

³F.M. Kirby Research Center for Functional Brain Imaging, Kennedy Krieger Research Institute, Baltimore, Maryland, USA.

Corresponding author:

Hanzhang Lu, Ph.D.

The Russell H. Morgan Department of Radiology and Radiological Science

Johns Hopkins University School of Medicine

600 N. Wolfe Street, Park 322

Baltimore, MD 21287

Email: hanzhang.lu@jhu.edu

Phone: 410-955-1431

Fax: 410-614-1977

Grant Sponsors: NIH R01 NS106702, NIH R01 NS106711, NIH R01 AG064792, NIH RF1 AG071515, NIH RF1 NS110041, NIH R21 AG058413, and NIH P41EB031771.

Word count: 7432

Submitted to Magnetic Resonance in Medicine

Abstract

The human brain constitutes 2% of the total body mass, but consumes 20% of the oxygen. The rate of the brain's oxygen utilization can be determined from the knowledge of cerebral blood flow and oxygen extraction fraction (OEF). Therefore, OEF is a key physiological parameter of the brain's function and metabolism. OEF has been suggested to be a useful biomarker in a number of brain diseases. With recent advances in MRI techniques, several MRI-based methods have been developed to measure OEF in the human brain. These MRI OEF techniques are based on T_2 of blood, phase of blood signal, susceptibility of blood-containing voxel, effect of deoxyhemoglobin on signal behavior in extravascular tissue, and calibration of BOLD signal using gas-inhalation. Compared to ^{15}O positron emission tomography, which is considered the "gold standard" for OEF measurement, MRI-based techniques are non-invasive, radiation-free, and have broader availabilities. This article provides a review of these emerging MRI-based OEF techniques. We first briefly introduce the role of OEF in brain oxygen homeostasis. We then review the methodological aspects of different categories of MRI OEF techniques, including their signal mechanisms, acquisition methods, and data analyses. Advantages and limitations of the techniques are discussed. Finally, we review key applications of these techniques in physiological and pathological conditions.

1. Introduction

The human brain constitutes 2% of the total body mass, but consumes 20% of the oxygen.¹ The brain has limited capacity to store oxygen, and its oxygen utilization primarily relies on the extraction from incoming arterial blood in real time. Therefore, oxygen extraction fraction (OEF) is a key physiological parameter of the brain's energy metabolism, and has been suggested to be a potential biomarker in several diseases, such as Alzheimer's disease (AD),^{2,3} carotid stenocclusive disease,⁴ sickle cell disease (SCD)^{5,6} and brain tumor.⁷

Measurement of OEF and the related cerebral metabolic rate of oxygen (CMRO₂) in humans used to be a niche market of positron emission tomography (PET) with ¹⁵O-labeled radiotracers.⁸⁻¹⁰ Although ¹⁵O-PET is still widely regarded as the gold standard for OEF and CMRO₂ mapping, its broad clinical applications have been hampered by the complex logistics, exposure to radiation, and the requirement for an onsite cyclotron to produce the ¹⁵O isotope, which has a short half-life of 2 minutes.

With the advances in MRI, several techniques have been developed to quantify OEF, based on the associations between blood oxygenation and MRI properties such as T₂,¹¹⁻¹³ susceptibility¹⁴⁻¹⁷ and magnetization phase,¹⁸⁻²¹ or by exploiting gas modulations.²²⁻²⁴ Among these techniques, some provide a global or whole-brain measure of OEF, while others aim to estimate OEF in specific brain regions. Some of these techniques have demonstrated potential clinical utility in brain diseases. The goal of this article is to provide a review of MRI-based OEF measurements. We will first introduce the physiological importance of OEF. We will then review major categories of MRI-based OEF techniques, including their signal mechanisms, acquisition methods, and data analyses. Finally, we will highlight key clinical applications of these techniques, although they are not meant to be exhaustive.

2. OEF and brain oxygen homeostasis

As illustrated in Figure 1, when fully oxygenated arterial blood flows through the capillaries, it releases oxygen to the surrounding tissues. The fraction of oxygen extracted by the tissue is OEF. Specifically, OEF is defined as:

$$OEF = \frac{Y_a - Y_v}{Y_a} \times 100\% \quad [1]$$

where Y_v is the venous oxygenation, defined as the fraction of oxyhemoglobin in the venous blood, and Y_a is the arterial oxygenation. Under normal conditions, $Y_a \approx 100\%$ and is relatively uniform throughout the body. Thus, OEF can often be simplified to:

$$OEF \approx 1 - Y_v \quad [2]$$

Y_a can also be conveniently measured by a pulse oximeter at the fingertip, especially when abnormalities in Y_a is expected. The major challenge is therefore the measurement of Y_v .

In blood, oxyhemoglobin and deoxyhemoglobin have distinct magnetic properties: oxyhemoglobin is diamagnetic, while deoxyhemoglobin is paramagnetic. Inside the vessel, increased concentration of deoxyhemoglobin causes a reduction in blood T_2 through water diffusion and exchange, similar to the well-known BOLD effect.¹¹⁻¹³ Higher concentration of deoxyhemoglobin also increases the magnetic susceptibility of voxels containing blood.^{14,25} This susceptibility difference between blood and tissue results in an additional phase angle in the transverse magnetization of blood.¹⁸⁻²¹ Outside the blood vessel, the local field inhomogeneity induced by the paramagnetic deoxyhemoglobin in the vessel networks results in additional decay of the tissue signal.^{26,27} Finally, BOLD signal changes during hypercapnic and hyperoxic gas inhalations can be modeled as a function of deoxyhemoglobin, and the non-linear nature of this function allows one to tease apart different variables and estimate OEF (among other physiological parameters).²²⁻²⁴ The OEF methods described in this review are based on one or more of the above-mentioned effects.

Once OEF is quantified, it can be combined with CBF to calculate $CMRO_2$ based on the Fick's principle:

$$CMRO_2 = CBF \cdot (Y_a - Y_v) \cdot C_{hb} \cdot [Hb] = CBF \cdot OEF \cdot Y_a \cdot C_{hb} \cdot [Hb] \quad [3]$$

where $[Hb]$ is the total hemoglobin concentration (in gram hemoglobin/dL blood). C_{hb} is the oxygen carrying capacity of hemoglobin (1.34mL or 59.8 μ mol O_2 /gram hemoglobin).²⁸ The term $(Y_a - Y_v) \cdot C_{hb} \cdot [Hb]$ is sometimes called the arterio-venous difference in oxygen content (AVDO₂). CBF can be measured globally by using phase-contrast MRI to quantify blood flow in the feeding arteries²⁹ or regionally by using arterial spin labeling (ASL) MRI.³⁰

It is worth noting that non-invasive quantification of OEF and $CMRO_2$ is also possible with MR spectroscopic imaging of ^{17}O , which is the only MR active stable isotope of oxygen. Due to the very low natural abundance of ^{17}O , ^{17}O MRI is typically performed with ^{17}O -enriched tracers.³¹⁻³⁶ Detailed review of ^{17}O MRI is beyond the scope of this article, and interested readers

are referred to other dedicated reviews.³⁴⁻³⁶ In this article, we will focus on MRI OEF techniques that do not require exogenous tracers.

3. MRI techniques for OEF measurement

3.1. T₂-based methods

3.1.1. Measurement of venous T₂

Under a fixed hematocrit (Hct) level, the blood oxygenation has a one-to-one correspondence to blood T₂.¹¹⁻¹³ Therefore, Y_v (and OEF) can be measured by quantifying its T₂.^{37,38} It is important to obtain pure venous blood signal in this measurement, as partial volume contamination from tissue or CSF can cause bias in T₂ determination. While some rely on high image resolution to separate blood signal in large cerebral veins,³⁹ more recent work sought to use special sequence design to isolate blood signal.

One example is T₂-relaxation-under-spin-tagging (TRUST) MRI.⁴⁰⁻⁴² As shown in Figure 2, TRUST labels blood spins on the venous side (Figure 2A), and uses the subtraction between control and labeled images (Figure 2B) to yield pure venous blood signal in the superior sagittal sinus (SSS). The venous blood T₂ is quantified by applying T₂-preparation with varying number of refocusing pulses, which is characterized by the effective TE (eTE).⁴⁰ The T₂-preparation pulses were applied to the entire brain, i.e., non-selectively, so that the degree of T₂ attenuation is not dependent on the flow velocity of the blood. Simple mono-exponential fitting of the blood signal as a function of eTE then yields venous T₂, which is converted to Y_v through a calibration model, based on the Hct level of the subject.⁴³ Since SSS drains the majority of cerebral cortex, TRUST MRI is thought to assess the global OEF level of the brain.

TRUST has a scan time of 1.2 min, and its signal mechanism is relatively straightforward. Rater dependence in TRUST data processing is minimal, as it uses the top signal voxels for T₂ estimation and the manual region-of-interest (ROI) plays a negligible role in the final result as long as it contains the SSS.⁴⁰ Test-retest reproducibility of TRUST MRI has been examined, with a same-day test-retest coefficient-of-variation (CoV) of 3%^{44,45} and a day-to-day CoV of 8% for OEF quantification.⁴⁴ The sensitivity of TRUST to OEF changes has been evaluated in several physiological challenges, such as caffeine ingestion,⁴⁶ hypercapnia,⁴⁷ hypoxia and hyperoxia,⁴⁸ all of which showed expected OEF changes using TRUST. The reliability of TRUST MRI has also been studied in the context of multiple sites⁴⁹ and different MR vendors.⁴⁵ In a recent study,

TRUST MRI was validated with ^{15}O -PET, which found a global OEF of $36.44 \pm 4.07\%$ with TRUST MRI and $36.45 \pm 3.65\%$ with ^{15}O -PET. The two modalities also revealed a correlation (intraclass correlation coefficient = 0.90) in OEF measures.⁴¹ Besides human studies, TRUST has also been implemented on animal MR imaging systems for OEF assessment in mice and rats.⁵⁰⁻⁵³

Other interesting technical work on global T_2 assessment include the use of high-spatial-resolution echo-planar or turbo-field-echo acquisition to obtain pure blood voxels,^{54,55} the combination of T_2 -preparation sequence with inversion recovery to simultaneously measure blood T_1 ,^{56,57} and the integration of flow measurement in the sequence to allow CMRO_2 measurement from a single sequence.⁵⁸ While global OEF estimation has the obvious limitation of lack of spatial information, these techniques tend to have a high reproducibility with a short scan duration, which makes it easy for them to be incorporated into the workflow of clinical or research imaging. The global OEF can also serve as a useful reference or validation measure for comparison with regional OEF techniques.

T_2 -based regional OEF techniques have also been reported. O'Brien et al. proposed to incorporate spatially selective saturation pulses into TRUST to isolate venous blood signal from localized regions of the brain, so that OEF can be measured for a specific hemisphere or a volume of interest.⁵⁹ Another technique, T_2 -relaxation-under-phase-contrast (TRUPC), employs phase-contrast complex subtraction to isolate flowing blood signal in the vessels.^{60,61} With this technique, OEF can be measured in regional cerebral veins, such as internal cerebral vein (ICV), the great vein of Galen, straight sinus, as well as pial veins.⁶⁰⁻⁶² TRUPC has a same-day CoV of 6% for OEF quantification.⁶⁰ An accelerated version of TRUPC has also been proposed,⁶² which shortens the acquisition time from 5 minutes to approximately 1 minute. TRUPC MRI has been validated against blood-gas oximetry of direct blood samples from the SSS on a piglet model.⁶³ Three-dimensional and T_2^* -based implementations of TRUPC have also been demonstrated.⁶⁴

Further advancement of T_2 -based methods attempted to provide voxel-wise OEF mapping. QUantitative Imaging of eXtraction of Oxygen and Tissue Consumption (QUIXOTIC)⁶⁵ and Velocity-Selective Excitation with Arterial Nulling (VSEAN)⁶⁶ are two techniques that use velocity-selective labeling or excitation to isolate post-capillary venous blood signal from tissues in the same voxel, allowing voxel-wise mapping of venous blood T_2 and OEF. However, since the post-capillary venous blood only comprises 1-3% of the volume of a voxel,⁶⁷ signal-to-noise-ratio (SNR) and partial volume contamination represent potential obstacles in clinical applications.

Approaches to shorten scan time,⁶⁸ enhance SNR and reduce CSF contamination⁶⁹ have been proposed.

3.1.2. T_2 -Y conversion

All T_2 -based oximetry methods require the use of a calibration model to convert the MR property of blood T_2 to the physiological parameter of oxygenation (Y). It should be noted that, under most circumstances, the same calibration plot can be used for different subjects and different studies. That is, one does not need to develop a calibration plot for each subject or each study. For applications in children and adults that have no hematological pathologies, the most commonly used T_2 -Y calibration model was proposed by Lu et al. (Figure 3),⁴³ which was based on in vitro experiments on bovine blood samples. Bovine blood has similar characteristics to adult human blood in terms of the hemoglobin structure, red blood cell (RBC) shape and size,⁷⁰ and diffusional water permeability.⁷¹ This bovine model has been demonstrated to provide Y_v and OEF quantifications consistent with ^{15}O -PET on healthy human adults.⁴¹

Some studies also considered the effect of Hct on the T_2 -Y relationship. Blood T_2 is indeed also dependent on Hct, although to a much less degree compared to oxygenation.⁴³ To take Hct into consideration in the conversion, one can use the calibration model to obtain Hct-specific T_2 -Y curve (most models provide a three-way relationship of Y, Hct, and T_2 ; thus, it is straightforward to obtain Hct-specific curves). Then, based on the individual's Hct value which is sometimes available in clinical workup or can be measured from a separate blood sampling or MRI sequence,^{72,73} one can use the proper T_2 -Y curve for the conversion (Figure 3B). When the individual Hct of the subject is unavailable, some studies have used 0.42 for males and 0.40 for females,^{74,75} accounting for some of the sex-related differences in Hct.

One limitation of the bovine model is that it was calibrated with a limited Hct range of 35%-55%.⁴³ Although this range is sufficient for most healthy volunteers and patients, extrapolation to anemic patients with very low Hct is somewhat controversial.^{63,76} This model may also be inappropriate for populations with atypical hemoglobin or RBCs. For example, in human neonates, the major type of hemoglobin is fetal hemoglobin (HbF), which has different structures than the adult hemoglobin (HbA).⁷⁷ A neonate-specific T_2 -Y calibration model has been reported.⁷⁸ Another example is SCD. Patients with SCD have sickle hemoglobin (HbS), which is highly unstable especially in its deoxygenated form, causing hemoglobin polymerization and

precipitation as well as RBC deformation (sickle appearance).⁷⁹ SCD patients can also have a considerable amount of HbF.^{54,80} Therefore, the magnetic property of sickled blood may be different from normal blood. SCD-specific T₂-Y calibration models have been reported.^{5,54,81} There is still much controversy in this area, but some of the SCD models have shown a substantial difference from the bovine model.⁵ One of the models further takes into account the varying percentage of HbS among SCD patients, especially those undergoing transfusion therapies.⁸¹ However, it should be pointed out that, while the differences associated with hemoglobin types have been hypothesized to be the main reason underlying disparities across models, it is also possible that experimental preparations (e.g. how temperature, pH, and cell integrity of the in vitro blood are controlled) and pulse sequences used (e.g. turbo-field-echo T₂ suffers from variations in magnetization across k lines and may under-estimate T₂ in SCD⁵⁴) may have contributed to some of these differences.

Future work should consider individual-specific, in vivo calibrations for patients with hematological conditions such as SCD. Such calibration can be conducted by applying MRI T₂ measurements to the superficial veins in the arm, for example, followed by blood sampling to obtain its oxygenation. A two-point (or multi-point) calibration can be further achieved by inducing oxygenation changes using arm compression to restrict blood flow or hyperoxic/hypoxic challenge. Such calibration data can then be applied to the brain venous T₂ to provide a more accurate estimation of OEF in the patient. Compared to previous calibration efforts, this approach can preserve erythrocytes' cell integrity and their nature shape in vivo, and will not have confounding factors related to blood preparation.

Finally, the above-mentioned models were primarily calibrated at 3T, with some conducted at 7T.⁸² Since T₂ varies with magnetic field strength, for applications at other field strengths, specific calibration models should be used.^{13,82-84} A unified calibration model based on quantitative theory and aggregated experiments has also been proposed.¹³

3.2. Phase-based methods

Because of the paramagnetic property of deoxyhemoglobin, the susceptibility difference ($\Delta\chi$) between blood and tissue has a linear relationship with the blood oxygenation:^{14,85,86}

$$\frac{\Delta\chi}{Hct} = \Delta\chi_{do}(1 - Y) + \Delta\chi_{oxy} \quad [4]$$

where $\Delta\chi_{do}$ is the susceptibility difference between fully oxygenated and deoxygenated blood, and has been characterized in the literature.^{14,80,85-87} $\Delta\chi_{oxy}$ is the susceptibility difference between fully oxygenated blood and tissue. $\Delta\chi_{oxy}$ is much smaller than $\Delta\chi_{do}$ ⁸⁵ and is often omitted in many studies. The susceptibility of blood induces local magnetic field offset ΔB_{bl} , which results in an additional phase difference $\Delta\Phi$ between successive echoes. Although in general the inverse problem to solve $\Delta\chi$ from $\Delta\Phi$ is complex and ill-conditioned,^{88,89} in a special case where the blood vessel can be modeled as a long straight cylinder approximately parallel to the main magnetic field B_0 , we have:²⁵

$$\Delta\Phi_{ie} = \Delta\varphi_{intra} - \Delta\varphi_{extra} \quad [5]$$

where $\Delta\varphi_{intra}$ and $\Delta\varphi_{extra}$ are the inter-echo phase difference within the vessel and in the neighboring extravascular tissue, respectively, and can be written as:

$$\Delta\varphi_{intra} = \gamma \cdot \Delta TE \cdot (\Delta B_{bl,intra} + \Delta B_{0,intra}) \quad [6]$$

$$\Delta\varphi_{extra} = \gamma \cdot \Delta TE \cdot (\Delta B_{bl,extra} + \Delta B_{0,extra}) \quad [7]$$

where γ is the gyromagnetic ratio and ΔTE is the TE difference between successive echoes. $\Delta B_{0,intra}$ and $\Delta B_{0,extra}$ are the intra- and extravascular background B_0 inhomogeneity, respectively. $\Delta B_{bl,intra}$ and $\Delta B_{bl,extra}$ are the blood-induced field inside and outside the vessel, respectively, and can be written as:²⁵

$$\Delta B_{bl,intra} = \frac{\Delta\chi}{2} \left(\cos^2 \theta - \frac{1}{3} \right) B_0 \quad [8]$$

$$\Delta B_{bl,extra} = \frac{\Delta\chi}{2} \left(\sin^2 \theta \cdot \frac{r^2}{\rho^2} \cdot \cos 2\omega \right) B_0 \quad [9]$$

where θ is the angle between the cylinder axis and B_0 , r is the vessel radius, ρ is the distance to the vessel axis, and ω is the azimuthal angle (Figure 4a). Assuming that the intra- and extravascular ROIs are sufficiently adjacent to each other thus the effects of background B_0 inhomogeneity, i.e., $\Delta B_{0,intra}$ and $\Delta B_{0,extra}$, are the same, $\Delta\Phi_{ie}$ is primarily related to the deoxyhemoglobin content in the blood. Figure 4b shows a simulated blood-induced field map (Eqs. [8,9]) for a hypothetical cylindrical vessel oriented at $\theta=20.1^\circ$.⁹⁰ It can be seen that the extravascular term, $\Delta B_{bl,extra}$, is very small when θ is small, and also decays rapidly with the distance from the vessel. Therefore, in most experimental studies where the vessel is approximately parallel to B_0 , $\Delta B_{bl,extra}$ is negligible and Eq. [5] can be written as:

$$\Delta\Phi_{ie} = \frac{\Delta\chi}{2} \left(\cos^2 \theta - \frac{1}{3} \right) B_0 \gamma \Delta TE \quad [10]$$

Note that θ can be measured from localizer or time-of-flight (TOF) vessel images.^{91,92} Combining Eqs. [4,10] and ignoring $\Delta\chi_{oxy}$, Y_v can be calculated by:²⁵

$$Y_v = 1 - \frac{2|\Delta\Phi_{ie}|}{\gamma B_0 \cdot \Delta TE \cdot \Delta\chi_{do} \cdot Hct \left(\cos^2 \theta - \frac{1}{3} \right)} \quad [11]$$

To quantify OEF using the phase-based method, gradient-recalled-echo (GRE) sequences with multiple TEs are typically used.^{18,19} Flow compensation is usually applied to minimize the flow-induced phase accumulation. Because the vessel is assumed to be a long straight cylinder, phase-based methods usually focus on large cerebral veins that are relatively parallel to B_0 , such as internal jugular veins (IJVs) and SSS,^{19,20,93} providing an estimation of global Y_v (and OEF) similar to the TRUST method. Figure 5 shows exemplar data of phase-based OEF at the level of SSS.⁹⁴ Some studies have also extended this technique to quantify OEF in selected regional veins that can be approximated as a long cylinder (length to diameter ratio > 5).^{18,21,95,96}

The accuracy of phase-based Y_v quantification relies on the calibration of $\Delta\chi_{do}$. For normal human adult blood, early works found a $\Delta\chi_{do}$ around 0.18 ppm (cgs units),¹⁴ while later studies reported $\Delta\chi_{do}$ to be 0.27 ppm (cgs).^{85,86} A recent study by Eldeniz et al. reported that $\Delta\chi_{do}$ was 0.19 ppm (cgs) for normal adult blood and the $\Delta\chi_{do}$ of sickled blood was not significantly different.⁸⁰ For human neonatal blood, Portnoy et al. found a $\Delta\chi_{do}$ of 0.21 ppm (cgs).⁸⁷

The sensitivity of phase-based methods to OEF changes have been demonstrated in various physiological challenges, such as hypercapnia,⁹³ hypoxia,⁹⁷ acetazolamide administration,^{98,99} caffeine ingestion⁹⁹ and breath-hold apnea.^{92,100}

Phase-based methods have been integrated with phase-contrast MRI to simultaneously measure global OEF and CBF levels in a single sequence dubbed OxFlow.²⁰ OxFlow has a CoV of 5% for global OEF quantification in same-day and day-to-day test-retest experiments.^{20,94} Recently, OxFlow has been demonstrated to provide global OEF values with no systematic bias compared to ¹⁵O-PET measurements on a porcine model.¹⁰¹ The original OxFlow sequence took 30 seconds.²⁰ With extensive acceleration, the variants of OxFlow can achieve a temporal resolution of a few seconds.^{92,100,102}

It should be noted that actual cerebral veins often exhibit curvature and noncircular cross-sections, thus rarely conform to the straight cylinder model. For example, SSS has a triangular

cross-section. Fortunately, it has been demonstrated that the absolute error in Y_v caused by non-circular cross-section is $< 5\%$ when the vessel tilt angle is small ($\theta < 30^\circ$).^{20,90,91} Alternatively, Driver et al. proposed to use a forward field calculation that takes into account the exact shape of the vessel to estimate Y_v .¹⁰³ Another major source of error is the phase errors induced by background B_0 inhomogeneities, which can be approximated as a second-order polynomial and then removed from the phase difference calculations in Eqs. [6,7].¹⁰⁴ In addition, to minimize partial-volume effects, sufficient image resolution is required. Finally, the processing of the data requires the manual drawing of extra- and intravascular ROIs, which need to be approached carefully to minimize rater dependence.

3.3. Methods based on quantitative susceptibility mapping

To estimate OEF in local veins with arbitrary orientation and geometry, quantitative susceptibility mapping (QSM) methods have been developed. QSM solves the general inverse problem to determine regional $\Delta\chi$ from $\Delta\Phi$. Under the assumption that the vein is at least one-voxel wide thus the $\Delta\chi$ measured is linearly proportional to blood oxygenation but not due to blood volume fraction, regional Y_v can be estimated using Eq. [4]. As mentioned earlier, this inverse problem is complex and ill-conditioned.^{88,89} Various algorithms have been proposed to solve this problem and quantify Y_v and OEF in local veins, such as thresholded k -space division¹⁵ and L1-regularization.^{16,105} To further correct for the flow-induced phase errors in the veins, an adaptive-quadratic fitting method has been proposed.¹⁰⁶ A potential caveat of these methods is that they may be sensitive to partial volume effects, i.e., the voxel is not 100% blood, which will result in an overestimation in venous oxygenation (thus underestimation in OEF), especially for small veins.^{15,16,25,107} Partial volume correction algorithms may be useful in improving the accuracy of OEF quantification.^{108,109}

Besides local veins, QSM-based methods have been extended to measure voxel-wise OEF.^{17,110} This method does not require the vein(s) to occupy the entire voxel. For an arbitrary voxel in the brain, its susceptibility has contributions from various sources including blood and non-blood tissues. To decouple these factors, one can acquire QSM and CBF (e.g., using ASL) in two isometabolic brain states to correct for the non-blood contributions (e.g., from tissue ferritin), which are assumed to remain the same between the two states. This has been carried out by using physiological challenges such as caffeine ingestion,¹⁷ hyperventilation,¹¹⁰ hypercapnia¹¹¹ or

hyperoxia.¹¹² These challenges are generally considered to be isometabolic (i.e., does not change $CMRO_2$), although controversial findings exist in the literature.^{46-48,58,93,113-117} The blood contribution arises from both venous and arterial blood and is modulated by their respective cerebral blood volume (CBV).^{17,110} In these methods,^{17,110-112} total CBV was estimated from CBF using relationships reported in the PET literature,^{118,119} and a certain ratio between arterial CBV and venous CBV (CBV_v) was assumed to separate out the venous susceptibility. Then, OEF at baseline and during physiological challenges can be quantified.^{17,110-112} Further development of QSM-based methods attempted to map OEF without any physiological challenges. For example, Zhang et al. proposed to estimate OEF from baseline QSM and CBF data by assuming $CMRO_2$ to have minimum local variance.¹²⁰ A caveat of these methods is the large number of assumptions, e.g., CBF-CBV relationship, arterial-venous CBV fractions, isometabolic challenge, and registration between EPI-based low-resolution ASL and GRE-based high-resolution QSM images. Additionally, the accuracy of the measurement is expected to strongly dependent on the reliability of the ASL CBF estimation in both baseline and challenged states, in the presence of confounding factors such as labeling efficiency, bolus arrival time, and arterial contaminations.¹²¹⁻¹²⁴

A few studies have compared QSM-based OEF measurements to PET-based OEF in healthy volunteers and in patients with arterial steno-occlusive diseases,¹²⁵⁻¹²⁸ in which the affected hemisphere is likely to have an elevated OEF. These studies showed significant correlations between QSM and PET in both the absolute OEF values and the affected/contralateral OEF ratio, although systematic biases were also reported.¹²⁵⁻¹²⁷

3.4. Quantitative BOLD

Unlike the T_2 -based and susceptibility-based methods that focus on the effect of blood oxygenation on “intravascular” signals, the quantitative BOLD (qBOLD) model focuses on the signal decay in the “extravascular” space due to the local field inhomogeneities induced by the paramagnetic deoxyhemoglobin in the vessel network. When studying the transverse signal decay due to deoxyhemoglobin, conventional BOLD models consider that the decay rate is related to both oxygenation level (i.e., OEF) and blood volume, but are unable to separate the effects of these two terms. That is, a faster BOLD signal decay could be due to either lower blood oxygenation or larger blood volume. Yablonskiy and colleagues, on the other hand, proposed a “static dephasing regime” BOLD model, in which the vessels were considered as an ensemble of randomly oriented

cylinders.²⁶ The key advantage of this model is that the oxygenation and blood volume effects can be separated experimentally. Specifically, two asymptotic equations can be derived to describe the signal behavior around a spin-echo:^{26,129,130}

$$\ln(S_S(\tau)) = \ln(S(0)) - (TE + \tau) \cdot R_2 - 0.3 \cdot DBV \cdot (\delta\omega \cdot \tau)^2, \text{ if } |\tau| < 1.5/\delta\omega \quad [12]$$

$$\ln(S_L(\tau)) = \ln(S(0)) - (TE + \tau) \cdot R_2 - R'_2|\tau| + DBV, \text{ if } |\tau| > 1.5/\delta\omega \quad [13]$$

where τ is the time gap between image acquisition and the spin-echo (τ is negative if the image is sampled before the spin-echo); S_S and S_L are the extravascular tissue signal for short and long τ , respectively; R_2 is the tissue transverse relaxation rate; DBV is the deoxygenated blood volume, which is mainly contributed to by the veins but also contains the part of capillary adjacent to the venous side. TE here is the time of the spin-echo. $\delta\omega$ is the deoxyhemoglobin induced frequency shift; R'_2 is the reversible transverse relaxation rate ($R'_2 = R_2^* - R_2$) and has the following relationship:^{26,129,130}

$$R'_2 = DBV \cdot \delta\omega = DBV \cdot \gamma \cdot \frac{4}{3} \pi \cdot \Delta\chi_{do} \cdot Hct \cdot (1 - Y_v) \cdot B_0 \quad [14]$$

Figure 6 shows a schematic of the qBOLD model.¹³⁰ The linear part of the model (Eq. [13]) is used to measure R'_2 , while the mismatch between the fitted linear intercept and the spin-echo signal allows estimation of DBV . OEF can then be calculated using Eq. [14].

To quantify OEF using the qBOLD model, many studies used a Gradient-Echo-Sampling-of-Spin-Echo (GESSE) sequence, in which multiple gradient echoes are acquired with varying τ from the spin-echo of a fixed TE .^{129,131-133} Figure 7 shows exemplar R'_2 , DBV and OEF maps acquired with GESSE-based qBOLD.¹³³ However, one drawback of this sequence is the varying R_2 -weighting among the gradient echo signals (Eq. [13]), which must be accounted for when quantifying R'_2 .¹³¹⁻¹³³ Alternatively, An et al. proposed an Asymmetric-Spin-Echo (ASE) sequence in which the position of the 180° refocusing pulse is varied to yield different τ while keeping $(TE+\tau)$ constant. This allows direct estimation of R'_2 without the confounding R_2 -weighting effects.¹³⁴

Both GESSE and ASE sequences allow OEF mapping within approximately 10 minutes.¹³⁰⁻¹³⁴ Reduction of scan time by using fast readout schemes has been proposed.¹³⁵ Sensitivity of ASE to OEF changes has been shown in carbogen inhalation challenge.¹³⁶ A recent study evaluated the test-rest reproducibility of an ASE-based method and showed a same-day CoV of $< 2\%$ and day-to-day CoV of $< 3\%$ for OEF averaged across gray matter, white matter, or whole-brain.¹³⁷ A few studies have evaluated the accuracy of qBOLD-based Y_v and OEF measurements

on rodent models, by comparing the Y_v in the SSS estimated by blood gas oximetry with the whole-brain averaged qBOLD-based Y_v .¹³⁸⁻¹⁴⁰ These studies demonstrated correlations between blood gas oximetry and qBOLD,¹³⁸⁻¹⁴⁰ but some also showed a bias.¹⁴⁰

Because the separation of the DBV and OEF effects in the qBOLD model relies on subtle differences in decay patterns (Eqs. [12,13]), accurate estimation of DBV and OEF from the GESSE or ASE signals requires high SNR.^{129,141,142} To address this problem, several groups developed a multiparametric-qBOLD (mqBOLD) scheme, in which CBV is measured using dynamic susceptibility contrast (DSC) MRI and R'_2 is estimated by separately mapping R_2 with a multiple spin-echo sequence and R_2^* by a multi-echo GRE sequence.¹⁴³⁻¹⁴⁵ However, the CBV measured by DSC is the total CBV rather than DBV. Therefore, the OEF produced by mqBOLD is a relative OEF.^{144,145} Alternatively, Stone et al. proposed to measure DBV through a hyperoxia challenge, while R'_2 was quantified using ASE.^{146,147} In this study, OEF values obtained with separate DBV measurement had substantially better agreement with TRUST global OEF than those obtained using DBV values estimated from the ASE signal.^{146,147} This manifested the importance of accurate DBV measurement in qBOLD-based OEF quantification.

A caveat of the qBOLD method is that the model described in Eqs. [12-14] considered a single extravascular tissue compartment and assumed that R'_2 is only related to the deoxygenated blood.^{26,129} However, in reality, R'_2 is also sensitive to macroscopic B_0 inhomogeneity, which must be corrected either prospectively using the z-shimming method,^{130,148} or retrospectively using a high-resolution field map¹³³ or by modeling the voxel spread function.^{149,150} An actual imaging voxel can also contain other compartments, such as intravascular blood and CSF or interstitial fluid (ISF). To address this issue, He et al. extended the original qBOLD model to incorporate the contributions from other compartments.¹³³ However, solving this multi-compartmental model requires prior knowledge about the tissue composition and results in a large number of fitting parameters.¹³³ Alternatively, one can minimize the contributions from other compartments to simplify the model. For example, the intravascular contribution can be reduced by using flow crushing gradients,¹³⁴ and the CSF/ISF signal can be suppressed by using a fluid-attenuated-inversion-recovery preparation pulse.¹³⁰ Another important assumption of the qBOLD model is “static dephasing”, i.e., neglecting the diffusion effects. However, it has been shown that diffusion introduces a vessel size dependent effect on the signal decay, and ignoring this diffusion effect may lead to systematic underestimation of OEF.¹⁵¹⁻¹⁵⁴

3.5. Dual-calibrated fMRI

BOLD-based fMRI is widely used to investigate the brain's function. It has also been applied to determine OEF when combined with gas inhalation physiological challenges. The R_2^* -weighted BOLD signal is dependent on CBV and the concentration of deoxyhemoglobin. Specifically, the relative BOLD signal change can be written as:^{155,156}

$$\frac{\Delta BOLD}{BOLD_0} = M \left(1 - \left(\frac{CBV_1}{CBV_0} \right) \left(\frac{[dHb]_1}{[dHb]_0} \right)^\beta \right) \quad [15]$$

where the parameter M is a composite constant related to field strength and TE, among other factors, and represents the maximum possible BOLD signal change that can be observed from the voxel. $[dHb]$ is the deoxyhemoglobin concentration. The subscript "0" denotes the baseline values while the subscript "1" denotes challenged state values. The constant β indicates the relationship between deoxyhemoglobin concentration and R_2^* , and is dependent on vascular morphology, water diffusion and the field strength, typically assumed to be 1.3 or 1.5 for 3T applications.^{22-24,155,157-159} Note that $[dHb]$ has the following relationship with Y_v :

$$[dHb] = [Hb](1 - Y_v) \quad [16]$$

where $[Hb]$ is the total hemoglobin concentration.

Eq. [15] is a general expression and is applicable to a variety of challenges such as task activation and physiological maneuvers. The dual-calibrated fMRI (dc-fMRI) OEF method applies this relationship to two gas inhalation regimes, hypercapnia and hyperoxia, to estimate Y_v (thereby OEF).

First, hypercapnia via CO_2 inhalation is employed to determine M . The MRI data acquisition involves the measurement of both BOLD and CBF (via ASL) at the baseline and during the hypercapnia challenge. The relative CBV change in Eq. [15] is then inferred from the relative CBF change by a power-law model:¹¹⁹

$$\frac{CBV_1}{CBV_0} = \left(\frac{CBF_1}{CBF_0} \right)^\alpha \quad [17]$$

The constant α was initially measured to be 0.38 for total CBV by Grubb et al.¹¹⁹ However, it is well known that BOLD signal is primarily modulated by CBV_v rather than total CBV. Later studies have confirmed the power-law relationship for CBV_v , but reported a substantially lower α value of ~ 0.2 .^{160,161}

Based on Eq. [3] mentioned earlier, assuming $Y_a=100\%$, and since $[Hb]$ and C_{hb} are unchanged with hypercapnia, $\frac{[dHb]_1}{[dHb]_0}$ can be rewritten as:

$$\frac{[dHb]_{hc}}{[dHb]_0} = \frac{CMRO_{2,hc}}{CMRO_{2,0}} \cdot \frac{CBF_0}{CBF_{hc}} \quad [18]$$

where the subscript ‘‘hc’’ denotes the values during hypercapnia. By combining Eqs. [15,17,18], it can be derived that:

$$\frac{\Delta BOLD_{hc}}{BOLD_0} = M \left(1 - \left(\frac{CBF_{hc}}{CBF_0} \right)^{\alpha-\beta} \left(\frac{CMRO_{2,hc}}{CMRO_{2,0}} \right)^\beta \right) \quad [19]$$

Under the assumption that hypercapnia is isometabolic ($CMRO_{2,hc}=CMRO_{2,0}$), M can then be estimated based on the hypercapnia-induced BOLD signal change and CBF change:

$$M = \frac{\Delta BOLD_{hc}}{BOLD_0} \cdot \frac{1}{1 - \left(\frac{CBF_{hc}}{CBF_0} \right)^{\alpha-\beta}} \quad [20]$$

Next, hyperoxia challenge is applied while BOLD and CBF changes are measured. To apply Eq. [15] to hyperoxia, $CMRO_2$ is again assumed to be unchanged and the $\frac{[dHb]_1}{[dHb]_0}$ term is rewritten as:²⁴

$$\frac{[dHb]_{ho}}{[dHb]_0} = \frac{CBF_0}{CBF_{ho}} - \frac{1}{[dHb]_0} \left\{ \frac{1}{C_{hb}} \left(C_aO_{2,ho} - \left(\frac{CBF_0}{CBF_{ho}} \right) C_aO_{2,0} \right) + [Hb] \left(\frac{CBF_0}{CBF_{ho}} - 1 \right) \right\} \quad [21]$$

where the subscript ‘‘ho’’ denotes the values during hyperoxia. C_{hb} is the oxygen carrying capacity of hemoglobin ($59.8\mu\text{mol O}_2/\text{gram hemoglobin}$).²⁸ C_aO_2 is the arterial oxygen content. Here C_aO_2 must consider the dissolved oxygen (which is no longer negligible), in addition to hemoglobin-bound oxygen, and can be written as:²⁴

$$C_aO_2 = C_{hb} \cdot [Hb] \cdot \frac{1}{\left(\frac{23400}{(P_aO_2)^3 + 150 \cdot P_aO_2} + 1 \right)} + P_aO_2 \cdot \varepsilon \quad [22]$$

where the first term represents O_2 bound to hemoglobin while the second term is the dissolved O_2 in blood plasma. P_aO_2 is the arterial oxygen partial pressure and can be approximated by the end-tidal oxygen partial pressure ($P_{ET}O_2$) measurement. ε is the coefficient of solubility of oxygen in blood ($0.138\mu\text{mol O}_2/\text{dL blood}/\text{mmHg O}_2$ tension).^{48,162} Finally, by combining Eqs. [2,15-17,20-22], we have:

$$OEF_0 = \frac{[dHb]_0}{[Hb]} = \frac{\frac{1}{C_{hb}} \cdot \frac{1}{[Hb]} \left(C_a O_{2,ho} - \left(\frac{CBF_0}{CBF_{ho}} \right) C_a O_{2,0} \right) + \left(\frac{CBF_0}{CBF_{ho}} - 1 \right)}{\frac{CBF_0}{CBF_{ho}} - \left(1 - \frac{\Delta BOLD_{ho}}{BOLD_0 \cdot M} \right)^{\frac{1}{\beta}} \left(\frac{CBF_0}{CBF_{ho}} \right)^{\frac{\alpha}{\beta}}} \quad [23]$$

Therefore, baseline OEF can be measured by acquiring BOLD signal, CBF and $P_{ET}O_2$ (to estimate C_aO_2 per Eq. [22]) at baseline and during two gas challenges: hypercapnia to calibrate M and hyperoxia to factor out $[dHb]_0$. A schematic of dc-fMRI experiments is shown in Figure 8.¹⁶³ The total duration of a dc-fMRI experiment is typically about 18 min.^{22-24,163}

To simultaneously acquire both BOLD and CBF images at the baseline and during gas challenges, one approach is to use an ASL sequence with a relatively long TE (~20ms) to increase the BOLD weighting. BOLD signal is then extracted by averaging adjacent ASL label and control images, while CBF is calculated from the label-control difference.²³ However, the TE used in this approach is suboptimal for both ASL and BOLD, leading to a compromised contrast-to-noise-ratio.¹⁶³ Later studies of dc-fMRI have mainly used dual- or multi-echo ASL sequences in which the CBF images are acquired at an early echo with shortest TE to maximize SNR, while the BOLD images are acquired at a later echo with optimal BOLD contrast.^{22,24,117,158,164,165} The dual-echo sequence contains greater cross-talks between the CBF and BOLD effects. Thus, some studies have used dual-excitation schemes in which a conventional ASL readout is immediately followed by another excitation to acquire BOLD images.¹⁶⁶⁻¹⁶⁸

Data processing of dc-fMRI is relatively complicated. One approach is to compute M and OEF_0 separately using the hypercapnia and hyperoxia data,²³ as described above, but may suffer from error propagations along the analysis pipeline. Alternatively, one can jointly estimate these parameters by fitting a generalized model using all data, which has been suggested to improve the robustness of OEF estimation.¹⁶⁹ Machine-learning based method has also been proposed.¹⁷⁰

dc-fMRI allows simultaneous measurement of OEF, CBF and $CMRO_2$. In addition, cerebrovascular reactivity (CVR) can also be extracted from the dc-fMRI data,^{23,169} which itself is an important index of cerebrovascular health.^{171,172} Figure 9 shows exemplar parametric maps produced by dc-fMRI.²³ The reproducibility of dc-fMRI measurements has been evaluated in two studies. Lajoie et al. reported a same-day CoV of 13.6% for OEF averaged across gray matter.¹⁷³ Merola et al. showed that the CoV of OEF averaged across gray matter was 6.7% and 10.5% for same-day and day-to-day test-retest experiments, respectively.¹⁷⁴ These CoV values are generally higher than some of the above-described methods. However, the advantage of the dc-fMRI method

is that it provides spatially resolved maps of multiple hemodynamic and metabolic parameters in one scan. The sensitivity of dc-fMRI to OEF changes has been demonstrated in caffeine challenges.¹¹⁷

A key assumption in dc-fMRI is that hypercapnia and hyperoxia do not change CMRO₂. However, it is under debate whether these two challenges are truly “isometabolic”.^{47,48,58,93,113-116} Simulations have demonstrated that violation of the isometabolic assumption results in bias in OEF estimation.^{175,176} Several approaches have been developed to account for possible alterations of CMRO₂ during gas challenges. Bulte et al. incorporated a fixed 10% reduction of CMRO₂ during hypercapnia in the model fitting.²³ Englund et al. proposed to measure global Y_v together with CBF and BOLD to relax the isometabolic mandate, assuming that Y_v changes induced by gas challenges are spatially uniform.¹⁷⁷ Driver et al. proposed to use graded hypercapnia to determine *M* and dose-wise CMRO₂ alterations.¹¹⁵

A limitation of dc-fMRI is the need of gas challenges, which require complex set-ups and can lead to a considerable dropout rate for patients due to the discomfort of hypercapnia challenge.¹⁶⁴ A recent study has proposed to replace gas challenges with breath-hold modulations to quantify OEF using the BOLD signal model.^{178,179}

Another limitation of the dc-fMRI method is that the reliability of the measure primarily hinges upon the quality of the ASL MRI data. ASL is known to suffer from low SNR even for basal perfusion measurement. The reliability of quantifying changes in CBF due to hypercapnia or hyperoxia requires further examination. Additionally, ASL signal may have confounding factors such as bolus arrival time, T₂^{*}, and labeling efficiency, which are also expected to alter during the physiological challenges.¹²¹⁻¹²⁴

3.6. Comparison and combination among techniques

Table 1 shows a brief summary of the techniques described in previous sections and their strengths and weaknesses. In general, global OEF measurements have high SNR and some of them, such as TRUST and OxFlow, have been extensively tested and validated against gold standards.^{20,41,44,45,49,94,101} For regional OEF measurement, a major challenge is the low SNR, because the local blood volume is very small and many techniques rely on complex model fittings that are sensitive to noise. Some have proposed to exploit machine learning methods to denoise

the OEF maps and reduce the computational cost.^{170,180,181} Future technical developments to improve the SNR is critical for the robustness of regional OEF measurement.

Several studies have compared the OEF values measured with different MRI-based techniques. For example, Barhoum et al. showed a significant correlation ($R^2=0.50$) between TRUST and OxFLOW Y_v measurements.⁹⁴ Significant correlations have also been reported between dc-fMRI and OxFLOW¹⁸² and between dc-fMRI and a QSM-based regional OEF method ($R^2=0.39$).¹⁸³ Overall, the correlations between different MRI methods were moderate and systematic differences in OEF quantification were observed.^{94,111,183-185}

Combinations of different MRI OEF techniques have been proposed.^{186,187} For example, Cho et al. combined the QSM model of the phase data and the qBOLD model of the magnitude data to estimate OEF from complex multi-echo GRE signals.¹⁸⁷⁻¹⁸⁹ One advantage of this QSM+qBOLD method is the joint estimation of the unknowns including Y_v , CBV_v , and non-blood susceptibility,¹⁸⁷ thus eliminating the assumptions needed in previous QSM methods.^{17,110-112,120} Figure 10 shows representative parametric maps generated by the QSM+qBOLD method.¹⁸⁷ Recently, this QSM+qBOLD method has been compared to ^{15}O -PET.¹²⁸ Although the averaged OEF values across subjects were not significantly different between QSM+qBOLD and ^{15}O -PET, there was no report of correlation between these two methods.¹²⁸

4. Clinical applications of MRI-based OEF

In the following sections, we will highlight several clinical applications of the MRI-based OEF techniques, although they are not meant to be exhaustive.

4.1. OEF across the human lifespan

A number of MRI studies have investigated the evolution of OEF from fetuses to elderly individuals.

For fetuses, a few studies used QSM-based methods to measure Y_v in the SSS in the fetal brain,¹⁹⁰⁻¹⁹⁴ and showed that the median Y_v across fetuses decreased from 67.5% in the second trimester to 60.8% in the third trimester.¹⁹³ Note that oxygen is delivered to the fetuses from the placenta through the umbilical vein, which was reported to have an average oxygenation of 84%.¹⁹⁵

For newborn infants, several MRI techniques have been adapted to measure OEF in the neonatal brain, including T_2 -based^{57,62,196-198} and phase-based¹⁹⁹ methods. In healthy neonates, Liu et al. reported an average global OEF of $31.8\pm 4.1\%$, which was similar to the adult OEF level.¹⁹⁷

There is currently a paucity of human studies on age-related OEF changes in children of 1 to 18 years of age. A previous ^{15}O -PET study found that OEF values in children were within the range of adult values regardless of the children's age.²⁰⁰

During adulthood, many MRI-based studies have reported an age-related increase in OEF,^{2,49,74,201-203} which was accompanied by a reduction in CBF.^{74,202,203} Results regarding CMRO₂ are mixed.^{74,202-204} Increase in OEF with age has also been suggested in recent studies using non-MRI techniques, such as ^{15}O -PET²⁰⁵ and near-infrared spectroscopy²⁰⁶⁻²⁰⁸ in human subjects.

4.2. Cognitive impairment

AD and vascular disease, as well as their co-occurrence, are the most common causes of cognitive impairment.²⁰⁹ There are some suggestions that OEF is differentially affected by AD and vascular disease.² For example, AD pathology will lead to diminished neural activities, and thereby decreased glucose and oxygen metabolism.²¹⁰ Thus, a decreased OEF is expected in the presence of relatively intact blood supply. On the other hand, small-vessel vascular pathology will cause a reduction in blood supply^{211,212} and result in an elevated oxygen extraction (Figure 11).² This notion is consistent with other recent MRI studies, which reported reduced OEF in cognitively impaired patients with minimal vascular risk factors.^{3,164} In addition, it has been shown that among cognitively normal individuals, the carriers of the apolipoprotein-E4 gene, a major genetic risk factor for AD, manifested diminished global OEF.⁷⁵

4.3. Cerebral large and small vessel diseases

In patients with unilateral stenosis/occlusion of major cerebral arteries, several MRI studies have reported an elevated OEF in the affected hemisphere,^{126,213-217} consistent with the “misery perfusion” pattern observed in previous ^{15}O -PET studies;^{4,218-220} while a few other MRI studies found insignificant hemispheric difference in OEF.²²¹⁻²²⁵ MRI techniques have also been used to evaluate OEF in patients before or after carotid stenting/endarterectomy.^{226,227}

In patients with Moyamoya disease, Watchmaker et al. found an elevated MRI-based global OEF,²²⁸ while ^{15}O -PET studies have reported mixed results.²²⁹⁻²³¹

In patients with cerebral small vessel disease, a recent MRI study found an elevated OEF in white matter and watershed regions, while the OEF in gray matter was decreased.²³²

4.4. Stroke

In acute ischemic stroke patients, a few MRI studies have reported that OEF was higher in the affected hemisphere than the contralateral side.²³³⁻²³⁵ A study by An et al. further attempted to delineate the stroke penumbra using MRI-based OEF and CBF measures.²³⁶ Several other MRI studies have found a decreased CMRO₂²³⁷⁻²³⁹ but increased OEF²⁴⁰ in the ischemic core of acute stroke patients.

A few studies reported an elevated R'_2 in ischemic tissues in acute stroke,²⁴¹⁻²⁴⁴ but did not quantify OEF. Because R'_2 is proportional to the product of OEF and DBV (see Section 3.4), consideration of DBV is crucial to assess the extent of OEF changes using the R'_2 data.²⁴¹

4.5. Sickle cell disease

A number of studies have investigated OEF changes in SCD but reported inconsistent results. Several groups have measured global OEF in SCD using T₂-based techniques,^{5,54,81,228,245-250} but the OEF results relied on the calibration model used to convert blood T₂ to Y_v (see Section 3.1.2).²⁵¹ Studies using the bovine calibration model⁴³ showed that OEF was higher in SCD patients than controls,^{228,245} and OEF was reduced after blood transfusion.²⁴⁶ In contrast, studies using the SCD-specific models^{5,81} have either reported a reduced OEF in SCD patients,^{5,247-249} or found no significant difference in OEF between SCD patients and controls.⁵⁴ One study used the neonatal calibration model,⁷⁸ and showed that elevated OEF was associated with impaired processing speed in SCD patients.²⁵⁰

Another group used ASE-based qBOLD methods and have consistently reported elevated whole-brain and regional OEF in children with SCD.^{6,252-255} In addition, in children receiving chronic transfusion therapy, CBF and OEF were reduced after transfusion, as shown in Figure 12.²⁵³

Two studies used susceptibility-based techniques, one found reduced OEF in the SSS,²⁵⁶ while another study showed elevated OEF in ICVs in SCD patients.²⁵⁷

The discrepancy in the literature suggests that the application of MRI-OEF techniques to pathological conditions with atypical RBC still presents some challenges. Future studies are needed to resolve the controversies in this field.

4.6. Brain injury

In neonates, hypoxic ischemic encephalopathy (HIE) is a leading cause of neonatal mortality and neurological disabilities.²⁵⁸ A few MRI-based studies have reported that neonates with HIE had lower OEF than controls,^{57,259} and neonates with severe HIE had even lower OEF than those with moderate HIE,²⁶⁰ which is presumably due to lower oxygen consumption rate.

In children and adults, traumatic brain injury (TBI) is among the most severe types of injury in terms of fatality and long-term impairment.²⁶¹ Several MRI-based studies have suggested that OEF was reduced in patients with TBI.²⁶²⁻²⁶⁶ In addition, in patients with TBI, a higher OEF predicted a better clinical outcome.²⁶²

4.7. OEF in physiological challenges

A number of studies have investigated the change of OEF and CMRO₂ under various physiological challenges, including hypercapnia,^{47,58,93,113-115,267} hypocapnia (e.g., induced by hyperventilation),^{110,113,268-270} hyperoxia,^{48,116,271,272} hypoxia,^{48,114,271,273-275} caffeine ingestion,^{17,46,99,117,276,277} acetazolamide injection^{99,248,278} and acute glucose ingestion.²⁷⁹ Table 2 summarizes the OEF, CBF and CMRO₂ changes under different physiological challenges.

4.8. Other applications

Elevated OEF was reported in patients with end-stage renal disease,²⁸⁰⁻²⁸² hepatic encephalopathy,²⁸³ systemic lupus erythematosus,²⁸⁴ refractory epilepsy²⁸⁵ and chronic cannabis usage.²⁸⁶ Increased OEF was also found in children with primary nocturnal enuresis²⁸⁷ and in preterm neonates with anemia.²⁸⁸

Reduced OEF was shown in patients with MELAS syndrome²⁸⁹ and multiple sclerosis,^{290,291} as well as in neonates with punctate white matter lesions.²⁹²

OEF and CMRO₂ have also been studied in patients with glioma,^{7,293-299} mountain sickness,²⁷⁴ cocaine addiction,³⁰⁰ anorexia,³⁰¹ bipolar disorder,³⁰² metabolic disorder³⁰³ and obstructive sleep apnea.^{304,305}

Besides disease-related changes, alterations of OEF and CMRO₂ have also been observed during natural sleep³⁰⁶ and after fatiguing aerobic exercise.³⁰⁷

Conclusions

This work provides an overview of emerging MRI techniques for OEF measurement. We reviewed the methodological aspects of different categories of MRI techniques, and discussed their advantages and limitations. We also briefly reviewed the applications of MRI-based OEF measurements in various physiological or pathological conditions. In summary, MRI-based OEF techniques provide a non-invasive assessment of the brain's function and metabolism, and have strong potentials in a variety of basic science and clinical applications.

References

1. Rolfe DF, Brown GC. Cellular energy utilization and molecular origin of standard metabolic rate in mammals. *Physiol Rev* 1997;77:731-758.
2. Jiang D, Lin Z, Liu P et al. Brain Oxygen Extraction Is Differentially Altered by Alzheimer's and Vascular Diseases. *J Magn Reson Imaging* 2020;52:1829-1837.
3. Thomas BP, Sheng M, Tseng BY, Tarumi T, Martin-Cook K, Womack KB, Cullum MC, Levine BD, Zhang R, Lu H. Reduced global brain metabolism but maintained vascular function in amnesic mild cognitive impairment. *J Cereb Blood Flow Metab* 2017;37:1508-1516.
4. Grubb RL, Jr., Derdeyn CP, Fritsch SM, Carpenter DA, Yundt KD, Videen TO, Spitznagel EL, Powers WJ. Importance of hemodynamic factors in the prognosis of symptomatic carotid occlusion. *JAMA* 1998;280:1055-1060.
5. Bush AM, Coates TD, Wood JC. Diminished cerebral oxygen extraction and metabolic rate in sickle cell disease using T2 relaxation under spin tagging MRI. *Magn Reson Med* 2018;80:294-303.
6. Fields ME, Williams KP, Ragan DK et al. Regional oxygen extraction predicts border zone vulnerability to stroke in sickle cell disease. *Neurology* 2018;90:e1134-e1142.
7. Stadlbauer A, Zimmermann M, Kitzwogger M, Oberndorfer S, Rossler K, Dorfler A, Buchfelder M, Heinz G. MR Imaging-derived Oxygen Metabolism and Neovascularization Characterization for Grading and IDH Gene Mutation Detection of Gliomas. *Radiology* 2017;283:799-809.
8. Mintun MA, Raichle ME, Martin WR, Herscovitch P. Brain oxygen utilization measured with O-15 radiotracers and positron emission tomography. *J Nucl Med* 1984;25:177-187.
9. Fan AP, An H, Moradi F, Rosenberg J, Ishii Y, Nariai T, Okazawa H, Zaharchuk G. Quantification of brain oxygen extraction and metabolism with [(15)O]-gas PET: A technical review in the era of PET/MRI. *Neuroimage* 2020;220:117136.
10. Baron JC, Jones T. Oxygen metabolism, oxygen extraction and positron emission tomography: Historical perspective and impact on basic and clinical neuroscience. *Neuroimage* 2012;61:492-504.

11. Thulborn KR, Waterton JC, Matthews PM, Radda GK. Oxygenation dependence of the transverse relaxation time of water protons in whole blood at high field. *Biochim Biophys Acta* 1982;714:265-270.
12. van Zijl PC, Eleff SM, Ulatowski JA, Oja JM, Ulug AM, Traystman RJ, Kauppinen RA. Quantitative assessment of blood flow, blood volume and blood oxygenation effects in functional magnetic resonance imaging. *Nat Med* 1998;4:159-167.
13. Li W, van Zijl PCM. Quantitative theory for the transverse relaxation time of blood water. *NMR Biomed* 2020;33:e4207.
14. Weisskoff RM, Kiihne S. MRI susceptometry: image-based measurement of absolute susceptibility of MR contrast agents and human blood. *Magn Reson Med* 1992;24:375-383.
15. Haacke EM, Tang J, Neelavalli J, Cheng YC. Susceptibility mapping as a means to visualize veins and quantify oxygen saturation. *J Magn Reson Imaging* 2010;32:663-676.
16. Fan AP, Bilgic B, Gagnon L, Witzel T, Bhat H, Rosen BR, Adalsteinsson E. Quantitative oxygenation venography from MRI phase. *Magn Reson Med* 2014;72:149-159.
17. Zhang J, Liu T, Gupta A, Spincemille P, Nguyen TD, Wang Y. Quantitative mapping of cerebral metabolic rate of oxygen (CMRO₂) using quantitative susceptibility mapping (QSM). *Magn Reson Med* 2015;74:945-952.
18. Haacke EM, Lai S, Reichenbach JR, Kuppusamy K, Hoogenraad FG, Takeichi H, Lin W. In vivo measurement of blood oxygen saturation using magnetic resonance imaging: a direct validation of the blood oxygen level-dependent concept in functional brain imaging. *Hum Brain Mapp* 1997;5:341-346.
19. Fernandez-Seara MA, Techawiboonwong A, Detre JA, Wehrli FW. MR susceptometry for measuring global brain oxygen extraction. *Magn Reson Med* 2006;55:967-973.
20. Jain V, Langham MC, Wehrli FW. MRI estimation of global brain oxygen consumption rate. *J Cereb Blood Flow Metab* 2010;30:1598-1607.
21. Fan AP, Benner T, Bolar DS, Rosen BR, Adalsteinsson E. Phase-based regional oxygen metabolism (PROM) using MRI. *Magn Reson Med* 2012;67:669-678.
22. Gauthier CJ, Hoge RD. Magnetic resonance imaging of resting OEF and CMRO(2) using a generalized calibration model for hypercapnia and hyperoxia. *Neuroimage* 2012;60:1212-1225.

23. Bulte DP, Kelly M, Germuska M, Xie J, Chappell MA, Okell TW, Bright MG, Jezzard P. Quantitative measurement of cerebral physiology using respiratory-calibrated MRI. *Neuroimage* 2012;60:582-591.
24. Wise RG, Harris AD, Stone AJ, Murphy K. Measurement of OEF and absolute CMRO₂: MRI-based methods using interleaved and combined hypercapnia and hyperoxia. *Neuroimage* 2013;83:135-147.
25. Wehrli FW, Fan AP, Rodgers ZB, Englund EK, Langham MC. Susceptibility-based time-resolved whole-organ and regional tissue oximetry. *NMR Biomed* 2017;30.
26. Yablonskiy DA, Haacke EM. Theory of NMR signal behavior in magnetically inhomogeneous tissues: the static dephasing regime. *Magn Reson Med* 1994;32:749-763.
27. Yablonskiy DA, Sukstanskii AL, He X. Blood oxygenation level-dependent (BOLD)-based techniques for the quantification of brain hemodynamic and metabolic properties - theoretical models and experimental approaches. *NMR Biomed* 2013;26:963-986.
28. Guyton AC, Hall JE. *Textbook of medical physiology* 11th ed. Elsevier Saunders 2006. doi:788-817.
29. Xu F, Ge Y, Lu H. Noninvasive quantification of whole-brain cerebral metabolic rate of oxygen (CMRO₂) by MRI. *Magn Reson Med* 2009;62:141-148.
30. Alsop DC, Detre JA, Golay X et al. Recommended implementation of arterial spin-labeled perfusion MRI for clinical applications: A consensus of the ISMRM perfusion study group and the European consortium for ASL in dementia. *Magn Reson Med* 2015;73:102-116.
31. Mellon EA, Beesam RS, Elliott MA, Reddy R. Mapping of cerebral oxidative metabolism with MRI. *Proc Natl Acad Sci U S A* 2010;107:11787-11792.
32. Kurzhunov D, Borowiak R, Reisert M, Joachim Krafft A, Caglar Ozen A, Bock M. 3D CMRO₂ mapping in human brain with direct (¹⁷O) MRI: Comparison of conventional and proton-constrained reconstructions. *Neuroimage* 2017;155:612-624.
33. Paech D, Nagel AM, Schultheiss MN et al. Quantitative Dynamic Oxygen ¹⁷ MRI at 7.0 T for the Cerebral Oxygen Metabolism in Glioma. *Radiology* 2020;295:181-189.
34. Zhu XH, Chen W. In vivo oxygen-17 NMR for imaging brain oxygen metabolism at high field. *Prog Nucl Magn Reson Spectrosc* 2011;59:319-335.

35. Zhu XH, Chen W. In vivo ¹⁷O MRS imaging - Quantitative assessment of regional oxygen consumption and perfusion rates in living brain. *Anal Biochem* 2017;529:171-178.
36. Gordji-Nejad A, Mollenhoff K, Oros-Peusquens AM, Pillai DR, Shah NJ. Characterizing cerebral oxygen metabolism employing oxygen-17 MRI/MRS at high fields. *MAGMA* 2014;27:81-93.
37. Wright GA, Hu BS, Macovski A. 1991 I.I. Rabi Award. Estimating oxygen saturation of blood in vivo with MR imaging at 1.5 T. *J Magn Reson Imaging* 1991;1:275-283.
38. Oja JM, Gillen JS, Kauppinen RA, Kraut M, van Zijl PC. Determination of oxygen extraction ratios by magnetic resonance imaging. *J Cereb Blood Flow Metab* 1999;19:1289-1295.
39. Golay X, Silvennoinen MJ, Zhou J, Clingman CS, Kauppinen RA, Pekar JJ, van Zijl PC. Measurement of tissue oxygen extraction ratios from venous blood T(2): increased precision and validation of principle. *Magn Reson Med* 2001;46:282-291.
40. Lu H, Ge Y. Quantitative evaluation of oxygenation in venous vessels using T2-Relaxation-Under-Spin-Tagging MRI. *Magn Reson Med* 2008;60:357-363.
41. Jiang D, Deng S, Franklin CG, O'Boyle M, Zhang W, Heyl BL, Pan L, Jerabek PA, Fox PT, Lu H. Validation of T2 -based oxygen extraction fraction measurement with (15) O positron emission tomography. *Magn Reson Med* 2021;85:290-297.
42. Xu F, Uh J, Liu P, Lu H. On improving the speed and reliability of T2-relaxation-under-spin-tagging (TRUST) MRI. *Magn Reson Med* 2012;68:198-204.
43. Lu H, Xu F, Grgac K, Liu P, Qin Q, van Zijl P. Calibration and validation of TRUST MRI for the estimation of cerebral blood oxygenation. *Magn Reson Med* 2012;67:42-49.
44. Liu P, Xu F, Lu H. Test-retest reproducibility of a rapid method to measure brain oxygen metabolism. *Magn Reson Med* 2013;69:675-681.
45. Jiang D, Liu P, Li Y, Mao D, Xu C, Lu H. Cross-vendor harmonization of T2 -relaxation-under-spin-tagging (TRUST) MRI for the assessment of cerebral venous oxygenation. *Magn Reson Med* 2018;80:1125-1131.
46. Xu F, Liu P, Pekar JJ, Lu H. Does acute caffeine ingestion alter brain metabolism in young adults? *Neuroimage* 2015;110:39-47.

47. Xu F, Uh J, Brier MR, Hart J, Jr., Yezhuvath US, Gu H, Yang Y, Lu H. The influence of carbon dioxide on brain activity and metabolism in conscious humans. *J Cereb Blood Flow Metab* 2011;31:58-67.
48. Xu F, Liu P, Pascual JM, Xiao G, Lu H. Effect of hypoxia and hyperoxia on cerebral blood flow, blood oxygenation, and oxidative metabolism. *J Cereb Blood Flow Metab* 2012;32:1909-1918.
49. Liu P, Dimitrov I, Andrews T et al. Multisite evaluations of a T2 -relaxation-under-spin-tagging (TRUST) MRI technique to measure brain oxygenation. *Magn Reson Med* 2016;75:680-687.
50. Wei Z, Xu J, Liu P, Chen L, Li W, van Zijl P, Lu H. Quantitative assessment of cerebral venous blood T2 in mouse at 11.7T: Implementation, optimization, and age effect. *Magn Reson Med* 2018;80:521-528.
51. Wei Z, Chen L, Hou X, van Zijl PCM, Xu J, Lu H. Age-Related Alterations in Brain Perfusion, Venous Oxygenation, and Oxygen Metabolic Rate of Mice: A 17-Month Longitudinal MRI Study. *Front Neurol* 2020;11:559.
52. Wei Z, Wang Q, Modi HR, Cho SM, Geocadin R, Thakor NV, Lu H. Acute-stage MRI cerebral oxygen consumption biomarkers predict 24-hour neurological outcome in a rat cardiac arrest model. *NMR Biomed* 2020;33:e4377.
53. Wei Z, Xu J, Chen L, Hirschler L, Barbier EL, Li T, Wong PC, Lu H. Brain metabolism in tau and amyloid mouse models of Alzheimer's disease: An MRI study. *NMR Biomed* 2021;34:e4568.
54. Li W, Xu X, Liu P, Strouse JJ, Casella JF, Lu H, van Zijl PCM, Qin Q. Quantification of whole-brain oxygenation extraction fraction and cerebral metabolic rate of oxygen consumption in adults with sickle cell anemia using individual T2 -based oxygenation calibrations. *Magn Reson Med* 2020;83:1066-1080.
55. Qin Q, Grgac K, van Zijl PC. Determination of whole-brain oxygen extraction fractions by fast measurement of blood T(2) in the jugular vein. *Magn Reson Med* 2011;65:471-479.
56. Petersen E, De Vis J, Alderliesten T, Kersbergen K, Benders M, Hendrikse J, van den Berg C. Simultaneous OEF and haematocrit assessment using T2 prepared blood

- relaxation imaging with inversion recovery. In Proceedings of Proc Intl Soc Mag Reson Med, 2012. p. 472.
57. De Vis JB, Petersen ET, Alderliesten T, Groenendaal F, de Vries LS, van Bel F, Benders MJ, Hendrikse J. Non-invasive MRI measurements of venous oxygenation, oxygen extraction fraction and oxygen consumption in neonates. *Neuroimage* 2014;95:185-192.
 58. Rodgers ZB, Englund EK, Langham MC, Magland JF, Wehrli FW. Rapid T2- and susceptometry-based CMRO₂ quantification with interleaved TRUST (iTRUST). *Neuroimage* 2015;106:441-450.
 59. O'Brien C, Okell TW, Chiew M, Jezzard P. Volume-localized measurement of oxygen extraction fraction in the brain using MRI. *Magn Reson Med* 2019;82:1412-1423.
 60. Krishnamurthy LC, Liu P, Ge Y, Lu H. Vessel-specific quantification of blood oxygenation with T2-relaxation-under-phase-contrast MRI. *Magn Reson Med* 2014;71:978-989.
 61. Krishnamurthy LC, Mao D, King KS, Lu H. Correction and optimization of a T2-based approach to map blood oxygenation in small cerebral veins. *Magn Reson Med* 2016;75:1100-1109.
 62. Jiang D, Lu H, Parkinson C, Su P, Wei Z, Pan L, Tekes A, Huisman T, Golden WC, Liu P. Vessel-specific quantification of neonatal cerebral venous oxygenation. *Magn Reson Med* 2019;82:1129-1139.
 63. Jiang D, Koehler RC, Liu X, Kulikowicz E, Lee JK, Lu H, Liu P. Quantitative validation of MRI mapping of cerebral venous oxygenation with direct blood sampling: A graded-O₂ study in piglets. *Magn Reson Med* 2021. doi: 10.1002/mrm.28786.
 64. Mao D, Li Y, Liu P, Peng SL, Pillai JJ, Lu H. Three-dimensional mapping of brain venous oxygenation using R₂* oximetry. *Magn Reson Med* 2018;79:1304-1313.
 65. Bolar DS, Rosen BR, Sorensen AG, Adalsteinsson E. QUantitative Imaging of eXtraction of oxygen and Tissue consumption (QUIXOTIC) using venular-targeted velocity-selective spin labeling. *Magn Reson Med* 2011;66:1550-1562.
 66. Guo J, Wong EC. Venous oxygenation mapping using velocity-selective excitation and arterial nulling. *Magn Reson Med* 2012;68:1458-1471.
 67. Hua J, Liu P, Kim T, Donahue M, Rane S, Chen JJ, Qin Q, Kim SG. MRI techniques to measure arterial and venous cerebral blood volume. *Neuroimage* 2019;187:17-31.

68. Stout JN, Adalsteinsson E, Rosen BR, Bolar DS. Functional oxygen extraction fraction (OEF) imaging with turbo gradient spin echo QUIXOTIC (Turbo QUIXOTIC). *Magn Reson Med* 2018;79:2713-2723.
69. Li W, Van Zijl P, Qin Q. Venous Oxygenation Mapping using Fourier-Transform based Velocity-Selective Pulse Trains. In Proceedings of the 29th Annual Meeting of ISMRM, 2021. p. 0472.
70. Wood D, Quiroz-Rocha G. Normal hematology of cattle. In: Weiss D, Wardrop K, editors. *Schalm's veterinary hematology*. 6th ed. doi. Ames: Blackwell Publishing; 2010. p 829-835.
71. Benga G, Borza T. Diffusional water permeability of mammalian red blood cells. *Comp Biochem Physiol B Biochem Mol Biol* 1995;112:653-659.
72. Qin Q, Strouse JJ, van Zijl PC. Fast measurement of blood T1 in the human jugular vein at 3 Tesla. *Magn Reson Med* 2011;65:1297-1304.
73. Xu F, Li W, Liu P, Hua J, Strouse JJ, Pekar JJ, Lu H, van Zijl PCM, Qin Q. Accounting for the role of hematocrit in between-subject variations of MRI-derived baseline cerebral hemodynamic parameters and functional BOLD responses. *Hum Brain Mapp* 2018;39:344-353.
74. Peng SL, Dumas JA, Park DC, Liu P, Filbey FM, McAdams CJ, Pinkham AE, Adinoff B, Zhang R, Lu H. Age-related increase of resting metabolic rate in the human brain. *Neuroimage* 2014;98:176-183.
75. Lin Z, Sur S, Soldan A et al. Brain Oxygen Extraction by Using MRI in Older Individuals: Relationship to Apolipoprotein E Genotype and Amyloid Burden. *Radiology* 2019;292:140-148.
76. Bush A, Borzage M, Detterich J, Kato RM, Meiselman HJ, Coates T, Wood JC. Empirical model of human blood transverse relaxation at 3 T improves MRI T2 oximetry. *Magn Reson Med* 2017;77:2364-2371.
77. Turgeon M. Erythrocyte morphology and inclusions. In: Turgeon M, editor. *Clinical hematology: theory and procedures*. 5th ed. doi. Philadelphia: Lippincott Williams & Wilkins; 2012. p 126-144.

78. Liu P, Chalak LF, Krishnamurthy LC, Mir I, Peng SL, Huang H, Lu H. T1 and T2 values of human neonatal blood at 3 Tesla: Dependence on hematocrit, oxygenation, and temperature. *Magn Reson Med* 2016;75:1730-1735.
79. Blanco A, Blanco G. Proteins. In: Blanco A, Blanco G, editors. *Medical Biochemistry*. doi: <https://doi.org/10.1016/B978-0-12-803550-4.00003-3>; Academic Press; 2017. p 21-71.
80. Eldeniz C, Binkley MM, Fields M, Guilliams K, Ragan DK, Chen Y, Lee JM, Ford AL, An H. Bulk volume susceptibility difference between deoxyhemoglobin and oxyhemoglobin for HbA and HbS: A comparative study. *Magn Reson Med* 2021;85:3383-3393.
81. Bush A, Vu C, Choi S, Borzage M, Miao X, Li W, Qin Q, Nederveen AJ, Coates TD, Wood JC. Calibration of T2 oximetry MRI for subjects with sickle cell disease. *Magn Reson Med* 2021;86:1019-1028.
82. Krishnamurthy LC, Liu P, Xu F, Uh J, Dimitrov I, Lu H. Dependence of blood T(2) on oxygenation at 7 T: in vitro calibration and in vivo application. *Magn Reson Med* 2014;71:2035-2042.
83. Silvennoinen MJ, Clingman CS, Golay X, Kauppinen RA, van Zijl PC. Comparison of the dependence of blood R2 and R2* on oxygen saturation at 1.5 and 4.7 Tesla. *Magn Reson Med* 2003;49:47-60.
84. Grgac K, Li W, Huang A, Qin Q, van Zijl PC. Transverse water relaxation in whole blood and erythrocytes at 3T, 7T, 9.4T, 11.7T and 16.4T; determination of intracellular hemoglobin and extracellular albumin relaxivities. *Magn Reson Imaging* 2017;38:234-249.
85. Jain V, Abdulmalik O, Probert KJ, Wehrli FW. Investigating the magnetic susceptibility properties of fresh human blood for noninvasive oxygen saturation quantification. *Magn Reson Med* 2012;68:863-867.
86. Spees WM, Yablonskiy DA, Oswald MC, Ackerman JJ. Water proton MR properties of human blood at 1.5 Tesla: magnetic susceptibility, T(1), T(2), T*(2), and non-Lorentzian signal behavior. *Magn Reson Med* 2001;45:533-542.
87. Portnoy S, Milligan N, Seed M, Sled JG, Macgowan CK. Human umbilical cord blood relaxation times and susceptibility at 3 T. *Magn Reson Med* 2018;79:3194-3206.

88. Deistung A, Schweser F, Reichenbach JR. Overview of quantitative susceptibility mapping. *NMR Biomed* 2017;30.
89. Wang Y, Liu T. Quantitative susceptibility mapping (QSM): Decoding MRI data for a tissue magnetic biomarker. *Magn Reson Med* 2015;73:82-101.
90. Li C, Langham MC, Epstein CL, Magland JF, Wu J, Gee J, Wehrli FW. Accuracy of the cylinder approximation for susceptometric measurement of intravascular oxygen saturation. *Magn Reson Med* 2012;67:808-813.
91. Langham MC, Magland JF, Epstein CL, Floyd TF, Wehrli FW. Accuracy and precision of MR blood oximetry based on the long paramagnetic cylinder approximation of large vessels. *Magn Reson Med* 2009;62:333-340.
92. Barhoum S, Langham MC, Magland JF, Rodgers ZB, Li C, Rajapakse CS, Wehrli FW. Method for rapid MRI quantification of global cerebral metabolic rate of oxygen. *J Cereb Blood Flow Metab* 2015;35:1616-1622.
93. Jain V, Langham MC, Floyd TF, Jain G, Magland JF, Wehrli FW. Rapid magnetic resonance measurement of global cerebral metabolic rate of oxygen consumption in humans during rest and hypercapnia. *J Cereb Blood Flow Metab* 2011;31:1504-1512.
94. Barhoum S, Rodgers ZB, Langham M, Magland JF, Li C, Wehrli FW. Comparison of MRI methods for measuring whole-brain venous oxygen saturation. *Magn Reson Med* 2015;73:2122-2128.
95. Hsieh CY, Cheng YC, Neelavalli J, Haacke EM, Stafford RJ. An improved method for susceptibility and radius quantification of cylindrical objects from MRI. *Magn Reson Imaging* 2015;33:420-436.
96. Hsieh CY, Cheng YN, Xie H, Haacke EM, Neelavalli J. Susceptibility and size quantification of small human veins from an MRI method. *Magn Reson Imaging* 2015;33:1191-1204.
97. Miao X, Nayak KS, Wood JC. In vivo validation of T2- and susceptibility-based Sv O₂ measurements with jugular vein catheterization under hypoxia and hypercapnia. *Magn Reson Med* 2019;82:2188-2198.
98. Zaitsev Y, Kudo K, Terae S, Yazu R, Ishizaka K, Fujima N, Tha KK, Haacke EM, Sasaki M, Shirato H. Mapping of cerebral oxygen extraction fraction changes with susceptibility-weighted phase imaging. *Radiology* 2011;261:930-936.

99. Buch S, Ye Y, Haacke EM. Quantifying the changes in oxygen extraction fraction and cerebral activity caused by caffeine and acetazolamide. *J Cereb Blood Flow Metab* 2017;37:825-836.
100. Rodgers ZB, Jain V, Englund EK, Langham MC, Wehrli FW. High temporal resolution MRI quantification of global cerebral metabolic rate of oxygen consumption in response to apneic challenge. *J Cereb Blood Flow Metab* 2013;33:1514-1522.
101. Narciso L, Ssali T, Liu L et al. A Noninvasive Method for Quantifying Cerebral Metabolic Rate of Oxygen by Hybrid PET/MRI: Validation in a Porcine Model. *J Nucl Med* 2021. doi: 10.2967/jnumed.120.260521.
102. Cao W, Chang YV, Englund EK, Song HK, Barhoum S, Rodgers ZB, Langham MC, Wehrli FW. High-speed whole-brain oximetry by golden-angle radial MRI. *Magn Reson Med* 2018;79:217-223.
103. Driver ID, Wharton SJ, Croal PL, Bowtell R, Francis ST, Gowland PA. Global intravascular and local hyperoxia contrast phase-based blood oxygenation measurements. *Neuroimage* 2014;101:458-465.
104. Langham MC, Magland JF, Floyd TF, Wehrli FW. Retrospective correction for induced magnetic field inhomogeneity in measurements of large-vessel hemoglobin oxygen saturation by MR susceptometry. *Magn Reson Med* 2009;61:626-633.
105. Fan AP, Evans KC, Stout JN, Rosen BR, Adalsteinsson E. Regional quantification of cerebral venous oxygenation from MRI susceptibility during hypercapnia. *Neuroimage* 2015;104:146-155.
106. Xu B, Liu T, Spincemaille P, Prince M, Wang Y. Flow compensated quantitative susceptibility mapping for venous oxygenation imaging. *Magn Reson Med* 2014;72:438-445.
107. McFadden JJ, Matthews JC, Scott LA, Parker GJM, Lohezic M, Parkes LM. Optimization of quantitative susceptibility mapping for regional estimation of oxygen extraction fraction in the brain. *Magn Reson Med* 2021;86:1314-1329.
108. Ward PG, Fan AP, Raniga P, Barnes DG, Dowe DL, Ng AC, Egan GF. Improved Quantification of Cerebral Vein Oxygenation Using Partial Volume Correction. *Front Neurosci* 2017;11:89.

109. McDaniel P, Bilgic B, Fan AP, Stout JN, Adalsteinsson E. Mitigation of partial volume effects in susceptibility-based oxygenation measurements by joint utilization of magnitude and phase (JUMP). *Magn Reson Med* 2017;77:1713-1727.
110. Zhang J, Zhou D, Nguyen TD, Spincemaille P, Gupta A, Wang Y. Cerebral metabolic rate of oxygen (CMRO₂) mapping with hyperventilation challenge using quantitative susceptibility mapping (QSM). *Magn Reson Med* 2017;77:1762-1773.
111. Ma Y, Sun H, Cho J, Mazerolle EL, Wang Y, Pike GB. Cerebral OEF quantification: A comparison study between quantitative susceptibility mapping and dual-gas calibrated BOLD imaging. *Magn Reson Med* 2020;83:68-82.
112. Ma Y, Mazerolle EL, Cho J, Sun H, Wang Y, Pike GB. Quantification of brain oxygen extraction fraction using QSM and a hyperoxic challenge. *Magn Reson Med* 2020;84:3271-3285.
113. Chen JJ, Pike GB. Global cerebral oxidative metabolism during hypercapnia and hypocapnia in humans: implications for BOLD fMRI. *J Cereb Blood Flow Metab* 2010;30:1094-1099.
114. Peng SL, Ravi H, Sheng M, Thomas BP, Lu H. Searching for a truly "iso-metabolic" gas challenge in physiological MRI. *J Cereb Blood Flow Metab* 2017;37:715-725.
115. Driver ID, Wise RG, Murphy K. Graded Hypercapnia-Calibrated BOLD: Beyond the Iso-metabolic Hypercapnic Assumption. *Front Neurosci* 2017;11:276.
116. Diringner MN, Aiyagari V, Zazulia AR, Videen TO, Powers WJ. Effect of hyperoxia on cerebral metabolic rate for oxygen measured using positron emission tomography in patients with acute severe head injury. *J Neurosurg* 2007;106:526-529.
117. Merola A, Germuska MA, Warnert EA, Richmond L, Helme D, Khot S, Murphy K, Rogers PJ, Hall JE, Wise RG. Mapping the pharmacological modulation of brain oxygen metabolism: The effects of caffeine on absolute CMRO₂ measured using dual calibrated fMRI. *Neuroimage* 2017;155:331-343.
118. Leenders KL, Perani D, Lammertsma AA et al. Cerebral blood flow, blood volume and oxygen utilization. Normal values and effect of age. *Brain* 1990;113 (Pt 1):27-47.
119. Grubb RL, Jr., Raichle ME, Eichling JO, Ter-Pogossian MM. The effects of changes in PaCO₂ on cerebral blood volume, blood flow, and vascular mean transit time. *Stroke* 1974;5:630-639.

120. Zhang J, Cho J, Zhou D, Nguyen TD, Spincemaille P, Gupta A, Wang Y. Quantitative susceptibility mapping-based cerebral metabolic rate of oxygen mapping with minimum local variance. *Magn Reson Med* 2018;79:172-179.
121. Aslan S, Xu F, Wang PL, Uh J, Yezhuvath US, van Osch M, Lu H. Estimation of labeling efficiency in pseudocontinuous arterial spin labeling. *Magn Reson Med* 2010;63:765-771.
122. Ho YC, Petersen ET, Zimine I, Golay X. Similarities and differences in arterial responses to hypercapnia and visual stimulation. *J Cereb Blood Flow Metab* 2011;31:560-571.
123. Heijtel DF, Mutsaerts HJ, Bakker E et al. Accuracy and precision of pseudo-continuous arterial spin labeling perfusion during baseline and hypercapnia: a head-to-head comparison with $(1)(5)O H(2)O$ positron emission tomography. *Neuroimage* 2014;92:182-192.
124. Donahue MJ, Faraco CC, Strother MK, Chappell MA, Rane S, Dethrage LM, Hendrikse J, Siero JC. Bolus arrival time and cerebral blood flow responses to hypercarbia. *J Cereb Blood Flow Metab* 2014;34:1243-1252.
125. Kudo K, Liu T, Murakami T et al. Oxygen extraction fraction measurement using quantitative susceptibility mapping: Comparison with positron emission tomography. *J Cereb Blood Flow Metab* 2016;36:1424-1433.
126. Uwano I, Kudo K, Sato R et al. Noninvasive Assessment of Oxygen Extraction Fraction in Chronic Ischemia Using Quantitative Susceptibility Mapping at 7 Tesla. *Stroke* 2017;48:2136-2141.
127. Fujimoto K, Uwano I, Sasaki M et al. Acetazolamide-Loaded Dynamic 7T MR Quantitative Susceptibility Mapping in Major Cerebral Artery Steno-Occlusive Disease: Comparison with PET. *AJNR Am J Neuroradiol* 2020;41:785-791.
128. Cho J, Lee J, An H, Goyal MS, Su Y, Wang Y. Cerebral oxygen extraction fraction (OEF): Comparison of challenge-free gradient echo QSM+qBOLD (QQ) with $(15)O$ PET in healthy adults. *J Cereb Blood Flow Metab* 2021;41:1658-1668.
129. Yablonskiy DA. Quantitation of intrinsic magnetic susceptibility-related effects in a tissue matrix. Phantom study. *Magn Reson Med* 1998;39:417-428.
130. Stone AJ, Blockley NP. A streamlined acquisition for mapping baseline brain oxygenation using quantitative BOLD. *Neuroimage* 2017;147:79-88.

131. An H, Lin W. Quantitative measurements of cerebral blood oxygen saturation using magnetic resonance imaging. *J Cereb Blood Flow Metab* 2000;20:1225-1236.
132. An H, Lin W. Cerebral oxygen extraction fraction and cerebral venous blood volume measurements using MRI: effects of magnetic field variation. *Magn Reson Med* 2002;47:958-966.
133. He X, Yablonskiy DA. Quantitative BOLD: mapping of human cerebral deoxygenated blood volume and oxygen extraction fraction: default state. *Magn Reson Med* 2007;57:115-126.
134. An H, Lin W. Impact of intravascular signal on quantitative measures of cerebral oxygen extraction and blood volume under normo- and hypercapnic conditions using an asymmetric spin echo approach. *Magn Reson Med* 2003;50:708-716.
135. Yin Y, Zhang Y, Gao JH. Dynamic measurement of oxygen extraction fraction using a multiecho asymmetric spin echo (MASE) pulse sequence. *Magn Reson Med* 2018;80:1118-1124.
136. An H, Sen S, Chen Y, Powers WJ, Lin W. Noninvasive Measurements of Cerebral Blood Flow, Oxygen Extraction Fraction, and Oxygen Metabolic Index in Human with Inhalation of Air and Carbogen using Magnetic Resonance Imaging. *Transl Stroke Res* 2012;3:246-254.
137. Ying C, Binkley MM, Kang P, Chen Y, Lee J, Ford AL, An H. Test–Retest Repeatability of Brain Oxygen Metabolism Measurement using MRI. In *Proceedings of the 29th Annual Meeting of ISMRM, 2021*. p. 4335.
138. He X, Zhu M, Yablonskiy DA. Validation of oxygen extraction fraction measurement by qBOLD technique. *Magn Reson Med* 2008;60:882-888.
139. An H, Liu Q, Chen Y, Lin W. Evaluation of MR-derived cerebral oxygen metabolic index in experimental hyperoxic hypercapnia, hypoxia, and ischemia. *Stroke* 2009;40:2165-2172.
140. Christen T, Lemasson B, Pannetier N, Farion R, Segebarth C, Remy C, Barbier EL. Evaluation of a quantitative blood oxygenation level-dependent (qBOLD) approach to map local blood oxygen saturation. *NMR Biomed* 2011;24:393-403.

141. Sedlacik J, Reichenbach JR. Validation of quantitative estimation of tissue oxygen extraction fraction and deoxygenated blood volume fraction in phantom and in vivo experiments by using MRI. *Magn Reson Med* 2010;63:910-921.
142. Sohlin MC, Schad LR. Theoretical prediction of parameter stability in quantitative BOLD MRI: dependence on SNR and sequence parameters. In Proceedings of the 17th Annual Meeting of ISMRM, 2009. p. 1623.
143. Christen T, Schmiedeskamp H, Straka M, Bammer R, Zaharchuk G. Measuring brain oxygenation in humans using a multiparametric quantitative blood oxygenation level dependent MRI approach. *Magn Reson Med* 2012;68:905-911.
144. Kaczmarz S, Gottler J, Zimmer C, Hyder F, Preibisch C. Characterizing white matter fiber orientation effects on multi-parametric quantitative BOLD assessment of oxygen extraction fraction. *J Cereb Blood Flow Metab* 2020;40:760-774.
145. Kaczmarz S, Hyder F, Preibisch C. Oxygen extraction fraction mapping with multi-parametric quantitative BOLD MRI: Reduced transverse relaxation bias using 3D-GraSE imaging. *Neuroimage* 2020;220:117095.
146. Stone AJ, Blockley NP. Improving qBOLD based measures of brain oxygenation using hyperoxia BOLD derived measures of blood volume. In Proceedings of the 25th Annual Meeting of ISMRM, 2017. p. 1658.
147. Stone AJ, Blockley NP. Improving qBOLD based measures of oxygen extraction fraction using hyperoxia-BOLD derived measures of blood volume. *bioRxiv* 2020. doi: 10.1101/2020.06.14.151134:2020.2006.2014.151134.
148. Blockley NP, Stone AJ. Improving the specificity of R2' to the deoxyhaemoglobin content of brain tissue: Prospective correction of macroscopic magnetic field gradients. *Neuroimage* 2016;135:253-260.
149. Ulrich X, Yablonskiy DA. Separation of cellular and BOLD contributions to T2* signal relaxation. *Magn Reson Med* 2016;75:606-615.
150. Yablonskiy DA, Sukstanskii AL, Luo J, Wang X. Voxel spread function method for correction of magnetic field inhomogeneity effects in quantitative gradient-echo-based MRI. *Magn Reson Med* 2013;70:1283-1292.

151. Dickson JD, Ash TW, Williams GB, Harding SG, Carpenter TA, Menon DK, Ansoorge RE. Quantitative BOLD: the effect of diffusion. *J Magn Reson Imaging* 2010;32:953-961.
152. Stone AJ, Holland NC, Berman AJL, Blockley NP. Simulations of the effect of diffusion on asymmetric spin echo based quantitative BOLD: An investigation of the origin of deoxygenated blood volume overestimation. *Neuroimage* 2019;201:116035.
153. Kiselev VG, Posse S. Analytical model of susceptibility-induced MR signal dephasing: effect of diffusion in a microvascular network. *Magn Reson Med* 1999;41:499-509.
154. Pannetier NA, Sohlin M, Christen T, Schad L, Schuff N. Numerical modeling of susceptibility-related MR signal dephasing with vessel size measurement: phantom validation at 3T. *Magn Reson Med* 2014;72:646-658.
155. Davis TL, Kwong KK, Weisskoff RM, Rosen BR. Calibrated functional MRI: mapping the dynamics of oxidative metabolism. *Proc Natl Acad Sci U S A* 1998;95:1834-1839.
156. Hoge RD, Atkinson J, Gill B, Crelier GR, Marrett S, Pike GB. Investigation of BOLD signal dependence on cerebral blood flow and oxygen consumption: the deoxyhemoglobin dilution model. *Magn Reson Med* 1999;42:849-863.
157. Bulte DP, Drescher K, Jezzard P. Comparison of hypercapnia-based calibration techniques for measurement of cerebral oxygen metabolism with MRI. *Magn Reson Med* 2009;61:391-398.
158. Gauthier CJ, Hoge RD. A generalized procedure for calibrated MRI incorporating hyperoxia and hypercapnia. *Hum Brain Mapp* 2013;34:1053-1069.
159. Bright MG, Croal PL, Blockley NP, Bulte DP. Multiparametric measurement of cerebral physiology using calibrated fMRI. *Neuroimage* 2019;187:128-144.
160. Chen JJ, Pike GB. BOLD-specific cerebral blood volume and blood flow changes during neuronal activation in humans. *NMR Biomed* 2009;22:1054-1062.
161. Chen JJ, Pike GB. MRI measurement of the BOLD-specific flow-volume relationship during hypercapnia and hypocapnia in humans. *Neuroimage* 2010;53:383-391.
162. Chiarelli PA, Bulte DP, Wise R, Gallichan D, Jezzard P. A calibration method for quantitative BOLD fMRI based on hyperoxia. *Neuroimage* 2007;37:808-820.
163. Germuska M, Wise RG. Calibrated fMRI for mapping absolute CMRO₂: Practicalities and prospects. *Neuroimage* 2019;187:145-153.

164. Lajoie I, Nugent S, Debacker C et al. Application of calibrated fMRI in Alzheimer's disease. *Neuroimage Clin* 2017;15:348-358.
165. Germuska M, Bulte DP. MRI measurement of oxygen extraction fraction, mean vessel size and cerebral blood volume using serial hyperoxia and hypercapnia. *Neuroimage* 2014;92:132-142.
166. Schmithorst VJ, Hernandez-Garcia L, Vannest J, Rajagopal A, Lee G, Holland SK. Optimized simultaneous ASL and BOLD functional imaging of the whole brain. *J Magn Reson Imaging* 2014;39:1104-1117.
167. Fernandez-Seara MA, Rodgers ZB, Englund EK, Wehrli FW. Calibrated bold fMRI with an optimized ASL-BOLD dual-acquisition sequence. *Neuroimage* 2016;142:474-482.
168. Germuska M, Chandler HL, Stickland RC, Foster C, Fasano F, Okell TW, Steventon J, Tomassini V, Murphy K, Wise RG. Dual-calibrated fMRI measurement of absolute cerebral metabolic rate of oxygen consumption and effective oxygen diffusivity. *Neuroimage* 2019;184:717-728.
169. Germuska M, Merola A, Murphy K, Babic A, Richmond L, Khot S, Hall JE, Wise RG. A forward modelling approach for the estimation of oxygen extraction fraction by calibrated fMRI. *Neuroimage* 2016;139:313-323.
170. Germuska M, Chandler H, Okell T, Fasano F, Tomassini V, Murphy K, Wise R. A frequency-domain machine learning method for dual-calibrated fMRI mapping of oxygen extraction fraction (OEF) and cerebral metabolic rate of oxygen consumption (CMRO₂). *Front Artif Intell* 2020;3.
171. Liu P, De Vis JB, Lu H. Cerebrovascular reactivity (CVR) MRI with CO₂ challenge: A technical review. *Neuroimage* 2019;187:104-115.
172. Juttukonda MR, Donahue MJ. Neuroimaging of vascular reserve in patients with cerebrovascular diseases. *Neuroimage* 2019;187:192-208.
173. Lajoie I, Tancredi FB, Hoge RD. Regional Reproducibility of BOLD Calibration Parameter M, OEF and Resting-State CMRO₂ Measurements with QUO₂ MRI. *PLoS One* 2016;11:e0163071.
174. Merola A, Germuska MA, Murphy K, Wise RG. Assessing the repeatability of absolute CMRO₂, OEF and haemodynamic measurements from calibrated fMRI. *Neuroimage* 2018;173:113-126.

175. Blockley NP, Griffeth VE, Stone AJ, Hare HV, Bulte DP. Sources of systematic error in calibrated BOLD based mapping of baseline oxygen extraction fraction. *Neuroimage* 2015;122:105-113.
176. Merola A, Murphy K, Stone AJ, Germuska MA, Griffeth VEM, Blockley NP, Buxton RB, Wise RG. Measurement of oxygen extraction fraction (OEF): An optimized BOLD signal model for use with hypercapnic and hyperoxic calibration. *Neuroimage* 2016;129:159-174.
177. Englund EK, Fernandez-Seara MA, Rodriguez-Soto AE, Lee H, Rodgers ZB, Vidorreta M, Detre JA, Wehrli FW. Calibrated fMRI for dynamic mapping of CMRO₂ responses using MR-based measurements of whole-brain venous oxygen saturation. *J Cereb Blood Flow Metab* 2020;40:1501-1516.
178. Germuska M, Stickland R, Chandler H, Wise R. A new method for mapping baseline cerebral oxygen metabolism using breath-hold calibrated fMRI. In *Proceedings of the 29th Annual Meeting of ISMRM*, 2021. p. 2684.
179. Germuska M, Stickland R, Chiarelli A, Chandler H, Wise R. Quantitative mapping of cerebral oxygen metabolism using breath-hold calibrated fMRI. *bioRxiv* 2021. doi: 10.1101/2021.04.08.438939:2021.2004.2008.438939.
180. Hubertus S, Thomas S, Cho J, Zhang S, Wang Y, Schad LR. Using an artificial neural network for fast mapping of the oxygen extraction fraction with combined QSM and quantitative BOLD. *Magn Reson Med* 2019;82:2199-2211.
181. Domsch S, Murle B, Weingartner S, Zapp J, Wenz F, Schad LR. Oxygen extraction fraction mapping at 3 Tesla using an artificial neural network: A feasibility study. *Magn Reson Med* 2018;79:890-899.
182. Chandler H, Germuska M, Okell T et al. Quantifying brain oxygen extraction fraction: correlation between a global venous susceptibility method and calibrated fMRI mapping method. In *Proceedings of the 26th Annual Meeting of ISMRM*, 2018. p. 4933.
183. Fan AP, Schafer A, Huber L, Lampe L, von Smuda S, Moller HE, Villringer A, Gauthier CJ. Baseline oxygenation in the brain: Correlation between respiratory-calibration and susceptibility methods. *Neuroimage* 2016;125:920-931.

184. Cho J, Ma Y, Spincemaille P, Pike GB, Wang Y. Cerebral oxygen extraction fraction: Comparison of dual-gas challenge calibrated BOLD with CBF and challenge-free gradient echo QSM+qBOLD. *Magn Reson Med* 2021;85:953-961.
185. Baas KPA, Coolen BF, Petersen ET, Biemond BJ, Strijkers GJ, Nederveen AJ. Comparative Analysis of Blood T2 Values Measured by T2 -TRIR and TRUST. *J Magn Reson Imaging* 2022. doi: 10.1002/jmri.28066.
186. Lee H, Englund EK, Wehrli FW. Interleaved quantitative BOLD: Combining extravascular R2' - and intravascular R2-measurements for estimation of deoxygenated blood volume and hemoglobin oxygen saturation. *Neuroimage* 2018;174:420-431.
187. Cho J, Kee Y, Spincemaille P, Nguyen TD, Zhang J, Gupta A, Zhang S, Wang Y. Cerebral metabolic rate of oxygen (CMRO₂) mapping by combining quantitative susceptibility mapping (QSM) and quantitative blood oxygenation level-dependent imaging (qBOLD). *Magn Reson Med* 2018;80:1595-1604.
188. Cho J, Zhang S, Kee Y, Spincemaille P, Nguyen TD, Hubertus S, Gupta A, Wang Y. Cluster analysis of time evolution (CAT) for quantitative susceptibility mapping (QSM) and quantitative blood oxygen level-dependent magnitude (qBOLD)-based oxygen extraction fraction (OEF) and cerebral metabolic rate of oxygen (CMRO₂) mapping. *Magn Reson Med* 2020;83:844-857.
189. Cho J, Spincemaille P, Nguyen TD, Gupta A, Wang Y. Temporal clustering, tissue composition, and total variation for mapping oxygen extraction fraction using QSM and quantitative BOLD. *Magn Reson Med* 2021. doi: 10.1002/mrm.28875.
190. Neelavalli J, Jella PK, Krishnamurthy U et al. Measuring venous blood oxygenation in fetal brain using susceptibility-weighted imaging. *J Magn Reson Imaging* 2014;39:998-1006.
191. Yadav BK, Buch S, Krishnamurthy U et al. Quantitative susceptibility mapping in the human fetus to measure blood oxygenation in the superior sagittal sinus. *Eur Radiol* 2019;29:2017-2026.
192. Yadav BK, Hernandez-Andrade E, Krishnamurthy U et al. Dual-Imaging Modality Approach to Evaluate Cerebral Hemodynamics in Growth-Restricted Fetuses: Oxygenation and Perfusion. *Fetal Diagn Ther* 2020;47:145-155.

193. Sun T, Qu F, Yadav B, Subramanian K, Jiang L, Haacke EM, Qian Z. Estimating cerebral venous oxygenation in human fetuses with ventriculomegaly using quantitative susceptibility mapping. *Magn Reson Imaging* 2021;80:21-25.
194. Yadav BK, Krishnamurthy U, Buch S et al. Imaging putative foetal cerebral blood oxygenation using susceptibility weighted imaging (SWI). *Eur Radiol* 2018;28:1884-1890.
195. Rodriguez-Soto AE, Langham MC, Abdulmalik O, Englund EK, Schwartz N, Wehrli FW. MRI quantification of human fetal O₂ delivery rate in the second and third trimesters of pregnancy. *Magn Reson Med* 2018;80:1148-1157.
196. Liu P, Huang H, Rollins N, Chalak LF, Jeon T, Halovanic C, Lu H. Quantitative assessment of global cerebral metabolic rate of oxygen (CMRO₂) in neonates using MRI. *NMR Biomed* 2014;27:332-340.
197. Liu P, Parkinson C, Jiang D, Ouyang M, De Vis JB, Northington FJ, Tekes A, Huang H, Huisman T, Golden WC. Characterization of MRI techniques to assess neonatal brain oxygenation and blood flow. *NMR Biomed* 2019;32:e4103.
198. Ferradal SL, Stout JN, Gagoski B, Vyas R, Ha C, Bolar DS, Cheng HH, Newburger J, Franceschini MA, Adalsteinsson E. Optimizing Unanesthetized Cerebral Oxygen Consumption Measures: Comparison of NIRS and MRI Approaches in Neonates with Congenital Heart Disease. In *Proceedings of Optical Tomography and Spectroscopy*, 2016. p. OM4C. 6.
199. Jain V, Buckley EM, Licht DJ et al. Cerebral oxygen metabolism in neonates with congenital heart disease quantified by MRI and optics. *J Cereb Blood Flow Metab* 2014;34:380-388.
200. Takahashi T, Shirane R, Sato S, Yoshimoto T. Developmental changes of cerebral blood flow and oxygen metabolism in children. *AJNR Am J Neuroradiol* 1999;20:917-922.
201. Jiang D, Lin Z, Liu P et al. Normal variations in brain oxygen extraction fraction are partly attributed to differences in end-tidal CO₂. *J Cereb Blood Flow Metab* 2020;40:1492-1500.
202. Lu H, Xu F, Rodrigue KM, Kennedy KM, Cheng Y, Flicker B, Hebrank AC, Uh J, Park DC. Alterations in cerebral metabolic rate and blood supply across the adult lifespan. *Cereb Cortex* 2011;21:1426-1434.

203. Catchlove SJ, Macpherson H, Hughes ME, Chen Y, Parrish TB, Pipingas A. An investigation of cerebral oxygen utilization, blood flow and cognition in healthy aging. *PLoS One* 2018;13:e0197055.
204. De Vis JB, Hendrikse J, Bhogal A, Adams A, Kappelle LJ, Petersen ET. Age-related changes in brain hemodynamics; A calibrated MRI study. *Hum Brain Mapp* 2015;36:3973-3987.
205. Aanerud J, Borghammer P, Chakravarty MM et al. Brain energy metabolism and blood flow differences in healthy aging. *J Cereb Blood Flow Metab* 2012;32:1177-1187.
206. Giacalone G, Zanoletti M, Contini D, Re R, Spinelli L, Roveri L, Torricelli A. Cerebral time domain-NIRS: reproducibility analysis, optical properties, hemoglobin species and tissue oxygen saturation in a cohort of adult subjects. *Biomed Opt Express* 2017;8:4987-5000.
207. Robu CB, Koninckx A, Docquier MA, Grosu I, De Kerchove L, Mastrobuoni S, Momeni M. Advanced Age and Sex Influence Baseline Regional Cerebral Oxygen Saturation as Measured by Near-Infrared Spectroscopy: Subanalysis of a Prospective Study. *J Cardiothorac Vasc Anesth* 2020;34:3282-3289.
208. Sun X, Ellis J, Corso PJ, Hill PC, Chen F, Lindsay J. Skin pigmentation interferes with the clinical measurement of regional cerebral oxygen saturation. *Br J Anaesth* 2015;114:276-280.
209. Schneider JA, Arvanitakis Z, Bang W, Bennett DA. Mixed brain pathologies account for most dementia cases in community-dwelling older persons. *Neurology* 2007;69:2197-2204.
210. Butterfield DA, Halliwell B. Oxidative stress, dysfunctional glucose metabolism and Alzheimer disease. *Nat Rev Neurosci* 2019;20:148-160.
211. Shi Y, Thrippleton MJ, Makin SD, Marshall I, Geerlings MI, de Craen AJM, van Buchem MA, Wardlaw JM. Cerebral blood flow in small vessel disease: A systematic review and meta-analysis. *J Cereb Blood Flow Metab* 2016;36:1653-1667.
212. Jann K, Shao X, Ma SJ et al. Evaluation of Cerebral Blood Flow Measured by 3D PCASL as Biomarker of Vascular Cognitive Impairment and Dementia (VCID) in a Cohort of Elderly Latinx Subjects at Risk of Small Vessel Disease. *Front Neurosci* 2021;15:627627.

213. Leatherday C, Dehkharghani S, Nahab F, Allen JW, Wu J, Hu R, Qiu D. Cerebral MR oximetry during acetazolamide augmentation: Beyond cerebrovascular reactivity in hemodynamic failure. *J Magn Reson Imaging* 2019;50:175-182.
214. Liu Z, Li Y. Cortical Cerebral Blood Flow, Oxygen Extraction Fraction, and Metabolic Rate in Patients with Middle Cerebral Artery Stenosis or Acute Stroke. *AJNR Am J Neuroradiol* 2016;37:607-614.
215. Xie S, Hui LH, Xiao JX, Zhang XD, Peng Q. Detecting misery perfusion in unilateral steno-occlusive disease of the internal carotid artery or middle cerebral artery by MR imaging. *AJNR Am J Neuroradiol* 2011;32:1504-1509.
216. Seiler A, Jurcoane A, Magerkurth J, Wagner M, Hattingen E, Deichmann R, Neumann-Haefelin T, Singer OC. T2' imaging within perfusion-restricted tissue in high-grade occlusive carotid disease. *Stroke* 2012;43:1831-1836.
217. Seiler A, Deichmann R, Pfeilschifter W, Hattingen E, Singer OC, Wagner M. T2-Imaging to Assess Cerebral Oxygen Extraction Fraction in Carotid Occlusive Disease: Influence of Cerebral Autoregulation and Cerebral Blood Volume. *PLoS One* 2016;11:e0161408.
218. Yamauchi H, Higashi T, Kagawa S, Nishii R, Kudo T, Sugimoto K, Okazawa H, Fukuyama H. Is misery perfusion still a predictor of stroke in symptomatic major cerebral artery disease? *Brain* 2012;135:2515-2526.
219. Derdeyn CP. Hemodynamics and oxygen extraction in chronic large artery steno-occlusive disease: Clinical applications for predicting stroke risk. *J Cereb Blood Flow Metab* 2018;38:1584-1597.
220. Gupta A, Baradaran H, Schweitzer AD, Kamel H, Pandya A, Delgado D, Wright D, Hurtado-Rua S, Wang Y, Sanelli PC. Oxygen extraction fraction and stroke risk in patients with carotid stenosis or occlusion: a systematic review and meta-analysis. *AJNR Am J Neuroradiol* 2014;35:250-255.
221. Gottler J, Kaczmarz S, Kallmayer M, Wustrow I, Eckstein HH, Zimmer C, Sorg C, Preibisch C, Hyder F. Flow-metabolism uncoupling in patients with asymptomatic unilateral carotid artery stenosis assessed by multi-modal magnetic resonance imaging. *J Cereb Blood Flow Metab* 2019;39:2132-2143.

222. Kaczmarz S, Gottler J, Petr J, Hansen MB, Mouridsen K, Zimmer C, Hyder F, Preibisch C. Hemodynamic impairments within individual watershed areas in asymptomatic carotid artery stenosis by multimodal MRI. *J Cereb Blood Flow Metab* 2021;41:380-396.
223. Eker OF, Ameli R, Makris N, Jurkovic T, Montigon O, Barbier EL, Cho TH, Nighoghossian N, Berthezene Y. MRI Assessment of Oxygen Metabolism and Hemodynamic Status in Symptomatic Intracranial Atherosclerotic Stenosis: A Pilot Study. *J Neuroimaging* 2019;29:467-475.
224. Bouvier J, Detante O, Tahon F et al. Reduced CMRO(2) and cerebrovascular reserve in patients with severe intracranial arterial stenosis: a combined multiparametric qBOLD oxygenation and BOLD fMRI study. *Hum Brain Mapp* 2015;36:695-706.
225. De Vis JB, Petersen ET, Bhogal A, Hartkamp NS, Klijn CJ, Kappelle LJ, Hendrikse J. Calibrated MRI to evaluate cerebral hemodynamics in patients with an internal carotid artery occlusion. *J Cereb Blood Flow Metab* 2015;35:1015-1023.
226. Seiler A, Kammerer S, Guhl A et al. Revascularization of High-Grade Carotid Stenosis Restores Global Cerebral Energy Metabolism. *Stroke* 2019;50:1742-1750.
227. Nomura JI, Uwano I, Sasaki M, Kudo K, Yamashita F, Ito K, Fujiwara S, Kobayashi M, Ogasawara K. Preoperative Cerebral Oxygen Extraction Fraction Imaging Generated from 7T MR Quantitative Susceptibility Mapping Predicts Development of Cerebral Hyperperfusion following Carotid Endarterectomy. *AJNR Am J Neuroradiol* 2017;38:2327-2333.
228. Watchmaker JM, Juttukonda MR, Davis LT et al. Hemodynamic mechanisms underlying elevated oxygen extraction fraction (OEF) in moyamoya and sickle cell anemia patients. *J Cereb Blood Flow Metab* 2018;38:1618-1630.
229. Kuroda S, Kashiwazaki D, Hirata K, Shiga T, Houkin K, Tamaki N. Effects of surgical revascularization on cerebral oxygen metabolism in patients with Moyamoya disease: an 15O-gas positron emission tomographic study. *Stroke* 2014;45:2717-2721.
230. Kaku Y, Iihara K, Nakajima N, Kataoka H, Fukuda K, Masuoka J, Fukushima K, Iida H, Hashimoto N. Cerebral blood flow and metabolism of hyperperfusion after cerebral revascularization in patients with moyamoya disease. *J Cereb Blood Flow Metab* 2012;32:2066-2075.

231. Iwama T, Akiyama Y, Morimoto M, Kojima A, Hayashida K. Comparison of positron emission tomography study results of cerebral hemodynamics in patients with bleeding- and ischemic-type moyamoya disease. *Neurosurg Focus* 1998;5:e3.
232. Kang P, Ying C, Chen Y, Ford A, An H, Lee J-M. White Matter and Watershed Ischemia in Cerebral Small Vessel Disease (95). *Neurology* 2021;96:95.
233. Xia S, Utriainen D, Tang J, Kou Z, Zheng G, Wang X, Shen W, Haacke EM, Lu G. Decreased oxygen saturation in asymmetrically prominent cortical veins in patients with cerebral ischemic stroke. *Magn Reson Imaging* 2014;32:1272-1276.
234. Luo Y, Gong Z, Zhou Y et al. Increased susceptibility of asymmetrically prominent cortical veins correlates with misery perfusion in patients with occlusion of the middle cerebral artery. *Eur Radiol* 2017;27:2381-2390.
235. Fan AP, Khalil AA, Fiebach JB, Zaharchuk G, Villringer A, Villringer K, Gauthier CJ. Elevated brain oxygen extraction fraction measured by MRI susceptibility relates to perfusion status in acute ischemic stroke. *J Cereb Blood Flow Metab* 2020;40:539-551.
236. An H, Ford AL, Chen Y et al. Defining the ischemic penumbra using magnetic resonance oxygen metabolic index. *Stroke* 2015;46:982-988.
237. Lee JM, Vo KD, An H, Celik A, Lee Y, Hsu CY, Lin W. Magnetic resonance cerebral metabolic rate of oxygen utilization in hyperacute stroke patients. *Ann Neurol* 2003;53:227-232.
238. Gersing AS, Ankenbrank M, Schwaiger BJ, Toth V, Janssen I, Kooijman H, Wunderlich S, Bauer JS, Zimmer C, Preibisch C. Mapping of cerebral metabolic rate of oxygen using dynamic susceptibility contrast and blood oxygen level dependent MR imaging in acute ischemic stroke. *Neuroradiology* 2015;57:1253-1261.
239. Zhang S, Cho J, Nguyen TD, Spincemille P, Gupta A, Zhu W, Wang Y. Initial Experience of Challenge-Free MRI-Based Oxygen Extraction Fraction Mapping of Ischemic Stroke at Various Stages: Comparison With Perfusion and Diffusion Mapping. *Front Neurosci* 2020;14:535441.
240. Stone AJ, Harston GWJ, Carone D, Okell TW, Kennedy J, Blockley NP. Prospects for investigating brain oxygenation in acute stroke: Experience with a non-contrast quantitative BOLD based approach. *Hum Brain Mapp* 2019;40:2853-2866.

241. Seiler A, Deichmann R, Noth U, Pfeilschifter W, Berkefeld J, Singer OC, Klein JC, Wagner M. Oxygenation-Sensitive Magnetic Resonance Imaging in Acute Ischemic Stroke Using T2'/R2' Mapping: Influence of Relative Cerebral Blood Volume. *Stroke* 2017;48:1671-1674.
242. Seiler A, Blockley NP, Deichmann R, Noth U, Singer OC, Chappell MA, Klein JC, Wagner M. The relationship between blood flow impairment and oxygen depletion in acute ischemic stroke imaged with magnetic resonance imaging. *J Cereb Blood Flow Metab* 2019;39:454-465.
243. Bauer S, Wagner M, Seiler A, Hattingen E, Deichmann R, Noth U, Singer OC. Quantitative T2'-mapping in acute ischemic stroke. *Stroke* 2014;45:3280-3286.
244. Geisler BS, Brandhoff F, Fiehler J, Saager C, Speck O, Rother J, Zeumer H, Kucinski T. Blood-oxygen-level-dependent MRI allows metabolic description of tissue at risk in acute stroke patients. *Stroke* 2006;37:1778-1784.
245. Jordan LC, Gindville MC, Scott AO et al. Non-invasive imaging of oxygen extraction fraction in adults with sickle cell anaemia. *Brain* 2016;139:738-750.
246. Juttukonda MR, Lee CA, Patel NJ et al. Differential cerebral hemometabolic responses to blood transfusions in adults and children with sickle cell anemia. *J Magn Reson Imaging* 2019;49:466-477.
247. Juttukonda MR, Donahue MJ, Waddle SL, Davis LT, Lee CA, Patel NJ, Pruthi S, Kassim AA, Jordan LC. Reduced oxygen extraction efficiency in sickle cell anemia patients with evidence of cerebral capillary shunting. *J Cereb Blood Flow Metab* 2021;41:546-560.
248. Vaclavu L, Petr J, Petersen ET, Mutsaerts H, Majoie CBL, Wood JC, VanBavel E, Nederveen AJ, Biemond BJ. Cerebral oxygen metabolism in adults with sickle cell disease. *Am J Hematol* 2020;95:401-412.
249. Vu C, Bush A, Choi S, Borzage M, Miao X, Nederveen AJ, Coates TD, Wood JC. Reduced global cerebral oxygen metabolic rate in sickle cell disease and chronic anemias. *Am J Hematol* 2021;96:901-913.
250. Prussien KV, Compas BE, Siciliano RE, Ciriegio AE, Lee CA, Kassim AA, DeBaun MR, Donahue MJ, Jordan LC. Cerebral Hemodynamics and Executive Function in Sickle Cell Anemia. *Stroke* 2021;52:1830-1834.

251. Lin Z, McIntyre T, Jiang D, Cannon A, Liu P, Tekes A, Casella JF, Slifer K, Lu H, Lance E. Brain oxygen extraction and metabolism in pediatric patients with sickle cell disease: comparison of four calibration models. *Frontiers in physiology* 2022. doi: 10.3389/fphys.2022.814979.
252. Fields ME, Williams KP, Ragan D, Eldeniz C, Binkley M, Hulbert ML, Vo KD, McKinstry R, Shimony J, An H. Elevations in MR measurements of whole brain and regional cerebral blood flow and oxygen extraction fraction suggest cerebral metabolic stress in children with sickle cell disease unaffected by overt stroke. doi: American Society of Hematology Washington, DC; 2015.
253. Williams KP, Fields ME, Ragan DK et al. Red cell exchange transfusions lower cerebral blood flow and oxygen extraction fraction in pediatric sickle cell anemia. *Blood* 2018;131:1012-1021.
254. Fields ME, Williams KP, Ragan D et al. Hydroxyurea reduces cerebral metabolic stress in patients with sickle cell anemia. *Blood* 2019;133:2436-2444.
255. Wang Y, Fella S, Fields ME et al. Cerebral Oxygen Metabolic Stress, Microstructural Injury, and Infarction in Adults With Sickle Cell Disease. *Neurology* 2021. doi: 10.1212/WNL.00000000000012404.
256. Croal PL, Leung J, Phillips CL, Serafin MG, Kassner A. Quantification of pathophysiological alterations in venous oxygen saturation: A comparison of global MR susceptometry techniques. *Magn Reson Imaging* 2019;58:18-23.
257. Shen J, Coates T, Wood JC. Lower Oxygen Saturation in the Internal Cerebral Vein of Patients with Sickle Cell Disease Revealed By Qsm-MRI. doi: American Society of Hematology Washington, DC; 2019.
258. Kurinczuk JJ, White-Koning M, Badawi N. Epidemiology of neonatal encephalopathy and hypoxic-ischaemic encephalopathy. *Early Hum Dev* 2010;86:329-338.
259. Jiang D, Golden WC, Parkinson C, Oishi K, Pan L, Lin Z, Lu H, Tekes A, Northington FJ, Liu P. Reduced brain oxygen extraction in hypoxic ischemic encephalopathy: association with 10min Apgar score. In *Proceedings of Pediatric Academic Societies Meeting*, 2020. p. E-PAS2020:2829.2484.
260. Shetty AN, Lucke AM, Liu P, Sanz Cortes M, Hagan JL, Chu ZD, Hunter JV, Lu H, Lee W, Kaiser JR. Cerebral oxygen metabolism during and after therapeutic hypothermia in

- neonatal hypoxic-ischemic encephalopathy: a feasibility study using magnetic resonance imaging. *Pediatr Radiol* 2019;49:224-233.
261. Brazinova A, Rehorcikova V, Taylor MS et al. Epidemiology of Traumatic Brain Injury in Europe: A Living Systematic Review. *J Neurotrauma* 2021;38:1411-1440.
 262. Ragan DK, McKinsty R, Benzinger T, Leonard J, Pineda JA. Depression of whole-brain oxygen extraction fraction is associated with poor outcome in pediatric traumatic brain injury. *Pediatr Res* 2012;71:199-204.
 263. Ragan DK, McKinsty R, Benzinger T, Leonard JR, Pineda JA. Alterations in cerebral oxygen metabolism after traumatic brain injury in children. *J Cereb Blood Flow Metab* 2013;33:48-52.
 264. Stone AJ, Lawrence TP, Okell TW, Voets NL, Blockley NP. Investigating tissue oxygenation in acute Traumatic Brain Injury using Arterial Spin Labelling and quantitative-BOLD. In *Proceedings of International Society for Magnetic Resonance in Medicine Annual Symposium, Paris, France, 2018*. p.
 265. Doshi H, Wiseman N, Liu J et al. Cerebral hemodynamic changes of mild traumatic brain injury at the acute stage. *PLoS One* 2015;10:e0118061.
 266. Chai C, Guo R, Zuo C, Fan L, Liu S, Qian T, Mark Haacke E, Xia S, Shen W. Decreased susceptibility of major veins in mild traumatic brain injury is correlated with post-concussive symptoms: A quantitative susceptibility mapping study. *Neuroimage Clin* 2017;15:625-632.
 267. Deckers PT, Bhogal AA, Dijsselhof MB, Faraco CC, Liu P, Lu H, Donahue MJ, Siero JCW. Hemodynamic and metabolic changes during hypercapnia with normoxia and hyperoxia using pCASL and TRUST MRI in healthy adults. *J Cereb Blood Flow Metab* 2021. doi: 10.1177/0271678X211064572:271678X211064572.
 268. Diringner MN, Videen TO, Yundt K, Zazulia AR, Aiyagari V, Dacey RG, Jr., Grubb RL, Powers WJ. Regional cerebrovascular and metabolic effects of hyperventilation after severe traumatic brain injury. *J Neurosurg* 2002;96:103-108.
 269. Coles JP, Fryer TD, Coleman MR et al. Hyperventilation following head injury: effect on ischemic burden and cerebral oxidative metabolism. *Crit Care Med* 2007;35:568-578.
 270. Diringner MN, Yundt K, Videen TO, Adams RE, Zazulia AR, Deibert E, Aiyagari V, Dacey RG, Jr., Grubb RL, Jr., Powers WJ. No reduction in cerebral metabolism as a

- result of early moderate hyperventilation following severe traumatic brain injury. *J Neurosurg* 2000;92:7-13.
271. Ainslie PN, Shaw AD, Smith KJ, Willie CK, Ikeda K, Graham J, Macleod DB. Stability of cerebral metabolism and substrate availability in humans during hypoxia and hyperoxia. *Clin Sci (Lond)* 2014;126:661-670.
272. Rockswold SB, Rockswold GL, Zaun DA, Zhang X, Cerra CE, Bergman TA, Liu J. A prospective, randomized clinical trial to compare the effect of hyperbaric to normobaric hyperoxia on cerebral metabolism, intracranial pressure, and oxygen toxicity in severe traumatic brain injury. *J Neurosurg* 2010;112:1080-1094.
273. Vestergaard MB, Lindberg U, Aachmann-Andersen NJ, Lisbjerg K, Christensen SJ, Law I, Rasmussen P, Olsen NV, Larsson HBW. Acute hypoxia increases the cerebral metabolic rate - a magnetic resonance imaging study. *J Cereb Blood Flow Metab* 2016;36:1046-1058.
274. Smith ZM, Krizay E, Guo J, Shin DD, Scadeng M, Dubowitz DJ. Sustained high-altitude hypoxia increases cerebral oxygen metabolism. *J Appl Physiol (1985)* 2013;114:11-18.
275. Moller K, Paulson OB, Hornbein TF, Colier WN, Paulson AS, Roach RC, Holm S, Knudsen GM. Unchanged cerebral blood flow and oxidative metabolism after acclimatization to high altitude. *J Cereb Blood Flow Metab* 2002;22:118-126.
276. Griffeth VE, Perthen JE, Buxton RB. Prospects for quantitative fMRI: investigating the effects of caffeine on baseline oxygen metabolism and the response to a visual stimulus in humans. *Neuroimage* 2011;57:809-816.
277. Perthen JE, Lansing AE, Liao J, Liu TT, Buxton RB. Caffeine-induced uncoupling of cerebral blood flow and oxygen metabolism: a calibrated BOLD fMRI study. *Neuroimage* 2008;40:237-247.
278. Vorstrup S, Henriksen L, Paulson OB. Effect of acetazolamide on cerebral blood flow and cerebral metabolic rate for oxygen. *J Clin Invest* 1984;74:1634-1639.
279. Xu F, Liu P, Pascual JM, Xiao G, Huang H, Lu H. Acute effect of glucose on cerebral blood flow, blood oxygenation, and oxidative metabolism. *Hum Brain Mapp* 2015;36:707-716.

280. Zheng G, Wen J, Lu H et al. Elevated global cerebral blood flow, oxygen extraction fraction and unchanged metabolic rate of oxygen in young adults with end-stage renal disease: an MRI study. *Eur Radiol* 2016;26:1732-1741.
281. Chai C, Liu S, Fan L, Liu L, Li J, Zuo C, Qian T, Haacke EM, Shen W, Xia S. Reduced deep regional cerebral venous oxygen saturation in hemodialysis patients using quantitative susceptibility mapping. *Metab Brain Dis* 2018;33:313-323.
282. Chai C, Wang H, Chu Z, Li J, Qian T, Mark Haacke E, Xia S, Shen W. Reduced regional cerebral venous oxygen saturation is a risk factor for the cognitive impairment in hemodialysis patients: a quantitative susceptibility mapping study. *Brain Imaging Behav* 2020;14:1339-1349.
283. Zheng G, Lu H, Yu W et al. Severity-specific alterations in CBF, OEF and CMRO₂ in cirrhotic patients with hepatic encephalopathy. *Eur Radiol* 2017;27:4699-4709.
284. Miyata M, Kakeda S, Kudo K, Iwata S, Tanaka Y, Wang Y, Korogi Y. Evaluation of oxygen extraction fraction in systemic lupus erythematosus patients using quantitative susceptibility mapping. *J Cereb Blood Flow Metab* 2019;39:1648-1658.
285. Ebrahimi T, Tafakhori A, Hashemi H, Ali Oghabian M. An interictal measurement of cerebral oxygen extraction fraction in MRI-negative refractory epilepsy using quantitative susceptibility mapping. *Phys Med* 2021;85:87-97.
286. Filbey FM, Aslan S, Lu H, Peng SL. Residual Effects of THC via Novel Measures of Brain Perfusion and Metabolism in a Large Group of Chronic Cannabis Users. *Neuropsychopharmacology* 2018;43:700-707.
287. Yu B, Huang M, Zhang X, Ma H, Peng M, Guo Q. Noninvasive imaging of brain oxygen metabolism in children with primary nocturnal enuresis during natural sleep. *Hum Brain Mapp* 2017;38:2532-2539.
288. Morris EA, Juttukonda MR, Lee CA, Patel NJ, Pruthi S, Donahue MJ, Jordan LC. Elevated brain oxygen extraction fraction in preterm newborns with anemia measured using noninvasive MRI. *J Perinatol* 2018;38:1636-1643.
289. Yu L, Xie S, Xiao J, Wang Z, Zhang X. Quantitative measurement of cerebral oxygen extraction fraction using MRI in patients with MELAS. *PLoS One* 2013;8:e79859.

290. Ge Y, Zhang Z, Lu H, Tang L, Jaggi H, Herbert J, Babb JS, Rusinek H, Grossman RI. Characterizing brain oxygen metabolism in patients with multiple sclerosis with T2-relaxation-under-spin-tagging MRI. *J Cereb Blood Flow Metab* 2012;32:403-412.
291. Fan AP, Govindarajan ST, Kinkel RP, Madigan NK, Nielsen AS, Benner T, Tinelli E, Rosen BR, Adalsteinsson E, Mainero C. Quantitative oxygen extraction fraction from 7-Tesla MRI phase: reproducibility and application in multiple sclerosis. *J Cereb Blood Flow Metab* 2015;35:131-139.
292. Qi Y, Liu P, Lin Z, Lu H, Wang X. Hemodynamic and Metabolic Assessment of Neonates With Punctate White Matter Lesions Using Phase-Contrast MRI and T2-Relaxation-Under-Spin-Tagging (TRUST) MRI. *Front Physiol* 2018;9:233.
293. Toth V, Forschler A, Hirsch NM, den Hollander J, Kooijman H, Gempt J, Ringel F, Schlegel J, Zimmer C, Preibisch C. MR-based hypoxia measures in human glioma. *J Neurooncol* 2013;115:197-207.
294. Saitta L, Heese O, Forster AF, Matschke J, Siemonsen S, Castellan L, Westphal M, Fiehler J, Goebell E. Signal intensity in T2' magnetic resonance imaging is related to brain glioma grade. *Eur Radiol* 2011;21:1068-1076.
295. Oughourlian TC, Yao J, Hagiwara A et al. Relative oxygen extraction fraction (rOEF) MR imaging reveals higher hypoxia in human epidermal growth factor receptor (EGFR) amplified compared with non-amplified gliomas. *Neuroradiology* 2021;63:857-868.
296. Wiestler B, Kluge A, Lukas M et al. Multiparametric MRI-based differentiation of WHO grade II/III glioma and WHO grade IV glioblastoma. *Sci Rep* 2016;6:35142.
297. Stadlbauer A, Mouridsen K, Doerfler A, Bo Hansen M, Oberndorfer S, Zimmermann M, Buchfelder M, Heinz G, Roessler K. Recurrence of glioblastoma is associated with elevated microvascular transit time heterogeneity and increased hypoxia. *J Cereb Blood Flow Metab* 2018;38:422-432.
298. Stadlbauer A, Zimmermann M, Doerfler A, Oberndorfer S, Buchfelder M, Coras R, Kitzwogerer M, Roessler K. Intratumoral heterogeneity of oxygen metabolism and neovascularization uncovers 2 survival-relevant subgroups of IDH1 wild-type glioblastoma. *Neuro Oncol* 2018;20:1536-1546.
299. Stadlbauer A, Kiefe TM, Eyupoglu I, Zimmermann M, Kitzwogerer M, Podar K, Buchfelder M, Heinz G, Oberndorfer S, Marhold F. Tissue Hypoxia and Alterations in

- Microvascular Architecture Predict Glioblastoma Recurrence in Humans. *Clin Cancer Res* 2021;27:1641-1649.
300. Liu P, Lu H, Filbey FM, Tamminga CA, Cao Y, Adinoff B. MRI assessment of cerebral oxygen metabolism in cocaine-addicted individuals: hypoactivity and dose dependence. *NMR Biomed* 2014;27:726-732.
301. Sheng M, Lu H, Liu P, Thomas BP, McAdams CJ. Cerebral perfusion differences in women currently with and recovered from anorexia nervosa. *Psychiatry Res* 2015;232:175-183.
302. Karthikeyan S, Fiksenbaum L, Grigorian A, Lu H, MacIntosh BJ, Goldstein BI. Normal Cerebral Oxygen Consumption Despite Elevated Cerebral Blood Flow in Adolescents With Bipolar Disorder: Putative Neuroimaging Evidence of Anomalous Energy Metabolism. *Front Psychiatry* 2019;10:739.
303. Pascual JM, Liu P, Mao D et al. Triheptanoin for glucose transporter type I deficiency (G1D): modulation of human ictogenesis, cerebral metabolic rate, and cognitive indices by a food supplement. *JAMA Neurol* 2014;71:1255-1265.
304. Rodgers ZB, Leinwand SE, Keenan BT, Kini LG, Schwab RJ, Wehrli FW. Cerebral metabolic rate of oxygen in obstructive sleep apnea at rest and in response to breath-hold challenge. *J Cereb Blood Flow Metab* 2016;36:755-767.
305. Wu PH, Rodriguez-Soto AE, Wiemken A, Englund EK, Rodgers ZB, Langham MC, Schwab RJ, Detre JA, Guo W, Wehrli FW. MRI evaluation of cerebral metabolic rate of oxygen (CMRO₂) in obstructive sleep apnea. *J Cereb Blood Flow Metab* 2022. doi: 10.1177/0271678X211071018:271678X211071018.
306. Caporale A, Lee H, Lei H, Rao H, Langham MC, Detre JA, Wu PH, Wehrli FW. Cerebral metabolic rate of oxygen during transition from wakefulness to sleep measured with high temporal resolution OxFlow MRI with concurrent EEG. *J Cereb Blood Flow Metab* 2021;41:780-792.
307. Bao D, Zhou J, Hao Y, Yang X, Jiao W, Hu Y, Wang X. The Effects of Fatiguing Aerobic Exercise on the Cerebral Blood Flow and Oxygen Extraction in the Brain: A Piloting Neuroimaging Study. *Front Neurol* 2019;10:654.
308. Bulte DP, Chiarelli PA, Wise RG, Jezzard P. Cerebral perfusion response to hyperoxia. *J Cereb Blood Flow Metab* 2007;27:69-75.

Table 1. Summary of MRI OEF techniques.

Method	Exemplar pulse sequences	Pros	Cons
T ₂ -based global	<ul style="list-style-type: none"> • TRUST⁴⁰ • T₂-TRIR⁵⁷ • High-resolution T₂ mapping⁵⁵ 	<ul style="list-style-type: none"> • High SNR • Short scan time • Straightforward data processing • Excellent reproducibility 	<ul style="list-style-type: none"> • Lack of spatial specificity • Dependence on T₂-Y calibration model
T ₂ -based regional	<ul style="list-style-type: none"> • TRUPC⁶² • QUIXOTIC⁶⁵ • VSEAN⁶⁶ 	<ul style="list-style-type: none"> • Vessel-specific or voxel-wise mapping of OEF 	<ul style="list-style-type: none"> • Low SNR • Dependence on T₂-Y calibration model
Phase-based global	<ul style="list-style-type: none"> • OxFlow²⁰ • Flow-compensated multi-echo GRE¹⁹ 	<ul style="list-style-type: none"> • High SNR • Very short scan time • Excellent reproducibility 	<ul style="list-style-type: none"> • Lack of spatial specificity • Restriction on vessel orientation and shape • Dependent on manual drawings of vessel and tissue ROI • $\Delta\chi_{do}$ of special RBC not fully characterized
QSM-based regional	<ul style="list-style-type: none"> • Flow-compensated multi-echo GRE¹⁵⁻¹⁷ 	<ul style="list-style-type: none"> • Vessel-specific or voxel-wise mapping of OEF 	<ul style="list-style-type: none"> • Susceptible to partial volume effect • Need of prior assumptions • Relatively long scan time
qBOLD	<ul style="list-style-type: none"> • GESSE¹³³ • ASE¹³⁴ 	<ul style="list-style-type: none"> • Voxel-wise mapping of OEF 	<ul style="list-style-type: none"> • Complex signal model • Confounding factors such as macroscopic field inhomogeneity • Relatively long scan time
dc-fMRI	<ul style="list-style-type: none"> • Dual-echo ASL^{22,24} 	<ul style="list-style-type: none"> • Voxel-wise mapping of OEF, CBF, CMRO₂ and CVR 	<ul style="list-style-type: none"> • Need of gas challenges • Complex signal model • Low SNR due to the need to measure ASL during baseline and challenged states • Long scan time

Table 2. OEF, CBF and CMRO₂ under physiological challenges.

Physiological challenge	CBF	OEF (or AVDO ₂)	CMRO ₂
Hypercapnia	Increased ^{47,58,93,113,114,267}	Decreased ^{47,58,93,113,114,267}	Mixed literature reporting decreased ^{47,114,115,267} or unchanged ^{93,113}
Hypocapnia	Decreased ^{110,113,268-270}	Increased ^{110,113,268-270}	Unchanged ^{110,113,268-270}
Hyperoxia	Decreased ^{48,308} or unchanged ^{116,271,272}	Unchanged ^{48,116,271,272}	Mixed literature reporting decreased, ⁴⁸ or unchanged ^{116,271,272}
Hypoxia	Increased ^{48,114,271,273,274} or unchanged ²⁷⁵	Unchanged ^{48,271,273-275}	Mixed literature reporting increased ^{48,114,273,274} or unchanged ^{271,275}
Caffeine	Decreased ^{17,46,99,117}	Increased ^{17,46,99,117}	Mixed literature reporting decreased, ¹¹⁷ increased ²⁷⁶ or unchanged ^{46,277}
Acetazolamide	Increased ^{99,248,278}	Decreased ^{99,248,278}	Unchanged ^{99,248,278}
Acute glucose ingestion	Unchanged ²⁷⁹	Decreased ²⁷⁹	Decreased ²⁷⁹

Figures

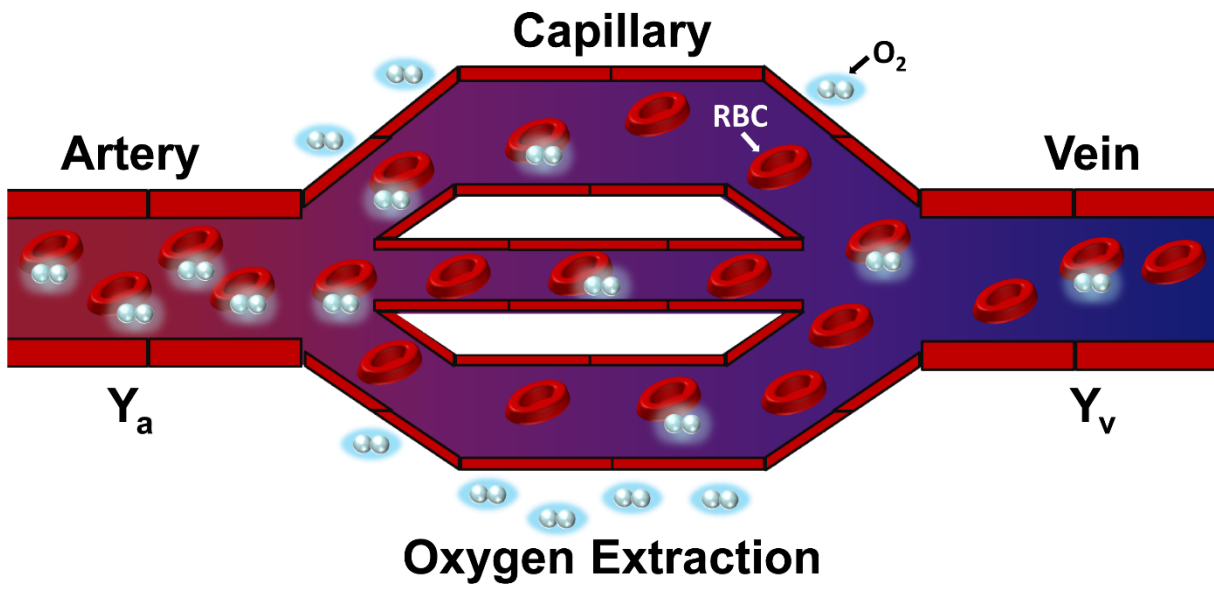


Figure 1. Illustration of oxygen extraction at the capillary bed.

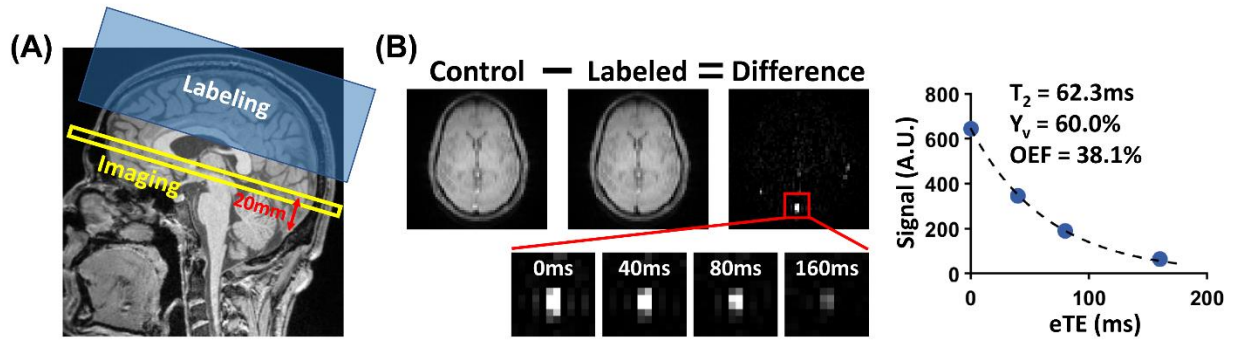


Figure 2. Illustration of TRUST MRI. (A) Position of TRUST MRI. Imaging slice (yellow box) is placed to be approximately parallel to the anterior-commissure–posterior-commissure line and 20mm above sinus confluence. Blue box represents the labeling slab. (B) Representative TRUST data. Subtraction between control and labeled images yields strong venous blood signal in the SSS (red box). The scatter plot shows venous signal as a function of eTEs. The resulting blood T_2 , Y_v , and OEF are also shown.

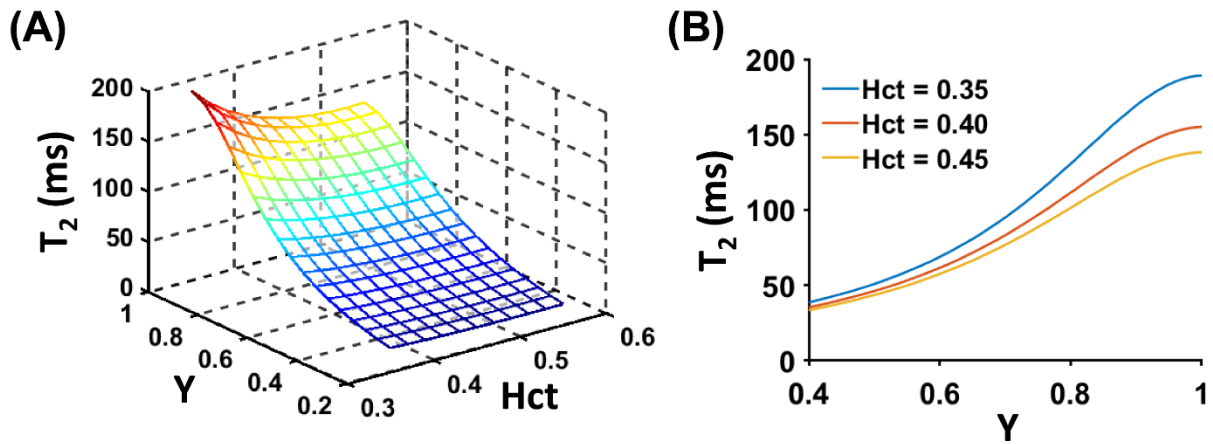


Figure 3. The bovine T_2 - Y calibration model. (A) 3D mesh plot showing the dependence of blood T_2 on Y and Hct; (B) Exemplar T_2 - Y conversion curves extracted from the 3D mesh plot. With a fixed Hct, T_2 increases monotonically with Y ; with a fixed Y , a lower Hct leads to a higher T_2 .

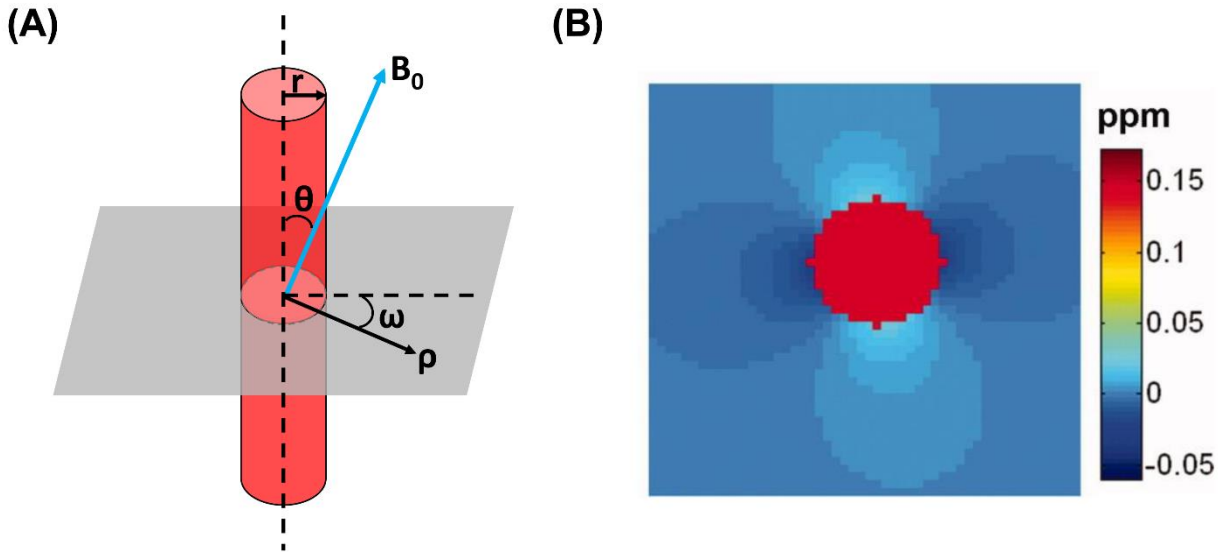


Figure 4. Blood-induced field of a cylindric vessel. (A) Illustration of the spatial relationship between the vessel and the variables in Eqs. [8,9]; (B) Simulated blood-induced field in a plane perpendicular to the vessel (gray parallelogram in [A]), assuming $Y_v=65\%$ and $\theta=20.1^\circ$. The induced field is represented in parts per million (ppm) with respect to B_0 . It is homogenous inside the vessel (red circle) and decays rapidly with the distance from the vessel. Adapted from Li et al.⁹⁰ with permission.

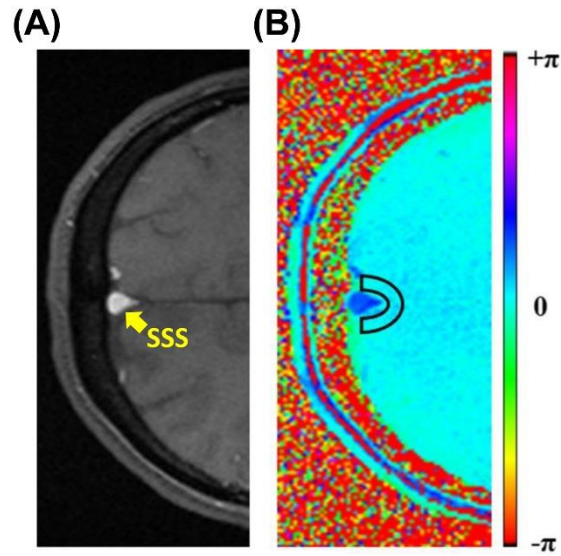


Figure 5. Exemplar data of phase-based OEF. Magnitude (A) and phase (B) images at the level of SSS (yellow arrow). The region-of-interest for extravascular tissue is denoted by the black box. Adapted from Barhoum et al.⁹⁴ with permission.

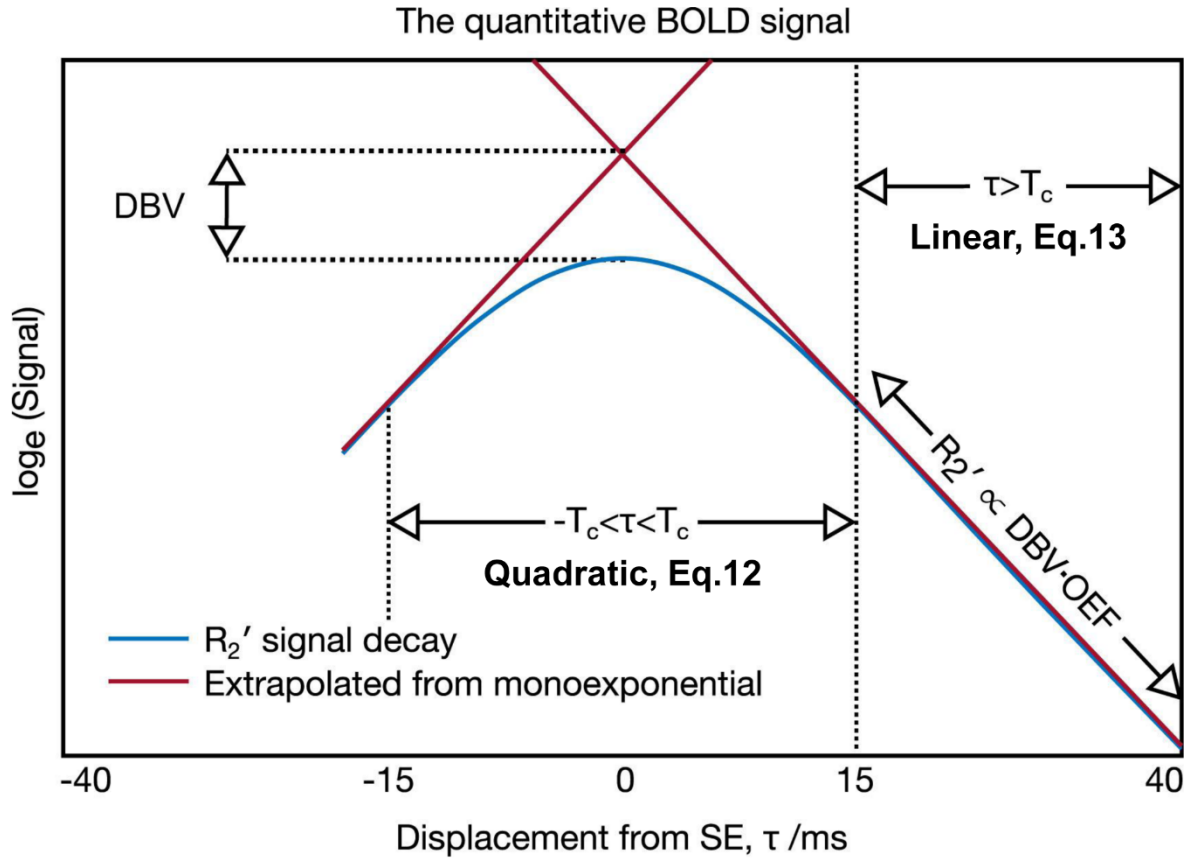


Figure 6. Schematic of the qBOLD model describing the transverse MR signal decay in the presence of a blood vessel network. R_2' is inferred from the monoexponential regime ($T_c = 1.5/\delta\omega$, Eq. [13]) and DBV is inferred from the mismatch between the linear intercept of this fit and the spin echo signal ($\tau=0\text{ms}$). Baseline OEF can then be estimated by combining these two measurements. Adapted from Stone et al.¹³⁰ with permission.

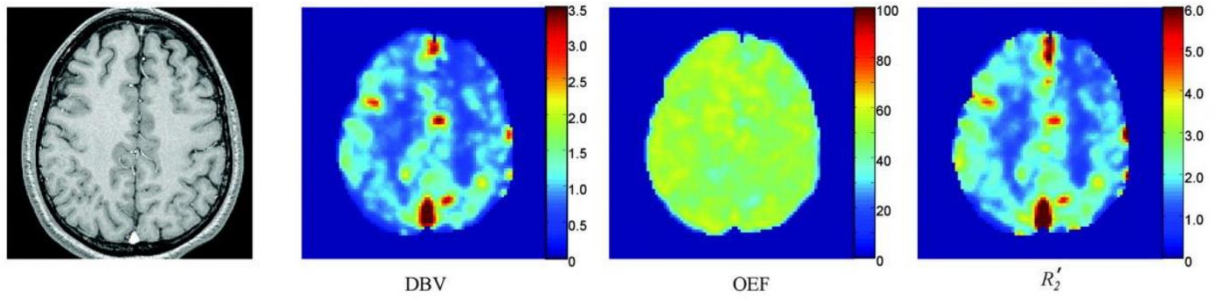


Figure 7. qBOLD parametric maps from a representative subject. DBV, OEF and R_2' maps are presented alongside an anatomic image. Adapted from He et al.¹³³ with permission.

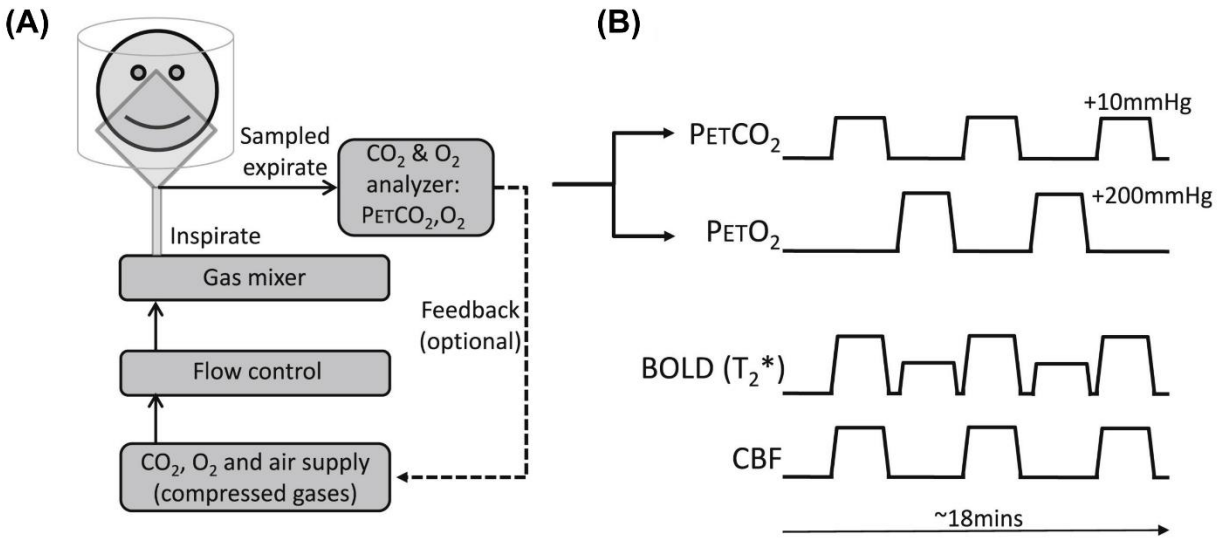


Figure 8. Schematic of dc-fMRI experiment. (A) Respiratory manipulations. (B) The corresponding idealized partial pressure of end-tidal CO_2 (P_{ETCO_2}), P_{ETO_2} , BOLD and CBF time-courses. Reproduced from Germuska et al.¹⁶³ with permission.

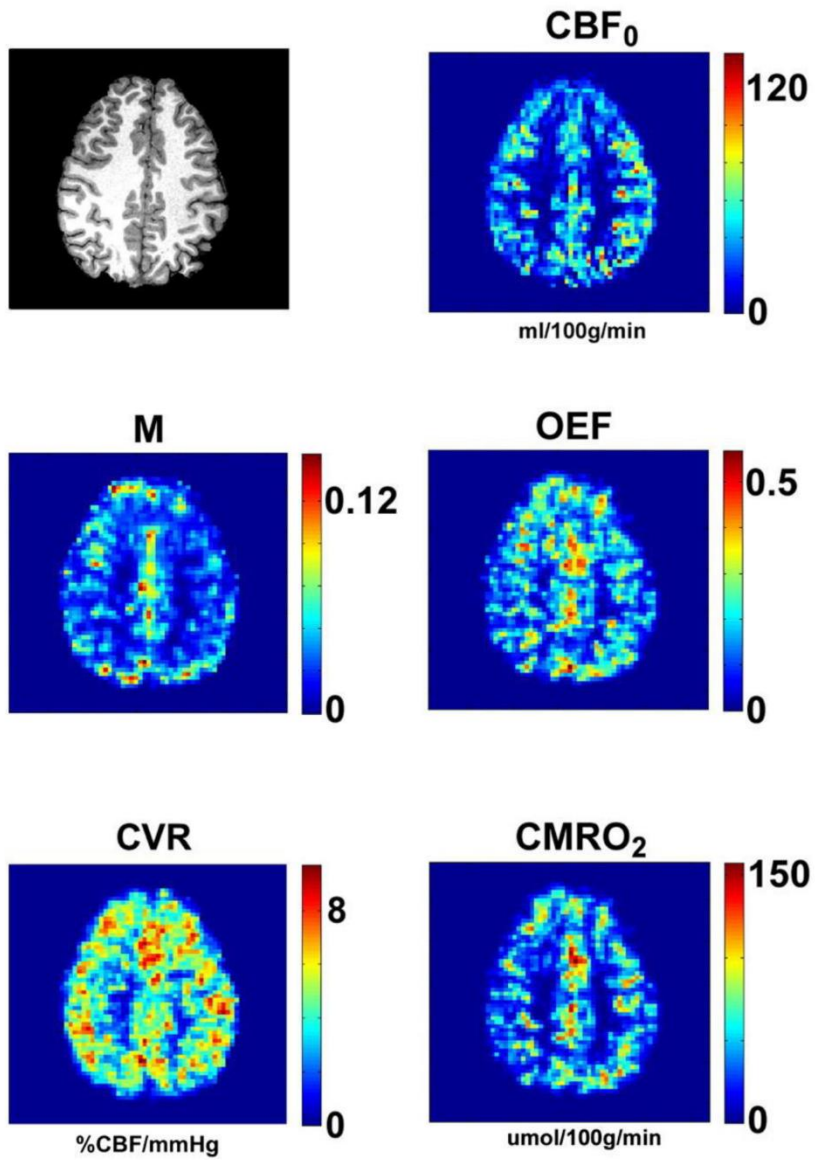


Figure 9. Exemplar parametric maps obtained with dc-fMRI. Adapted from Bulte et al.²³ with permission.

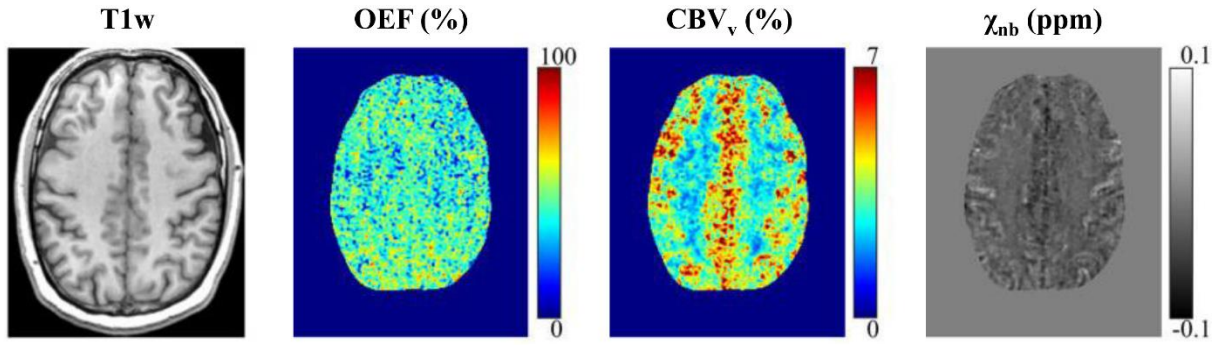


Figure 10. Representative OEF, venous cerebral blood volume (CBV_v) and non-blood susceptibility (χ_{nb}) maps generated by the QSM+qBOLD model. Adapted from Cho et al.¹⁸⁷ with permission.

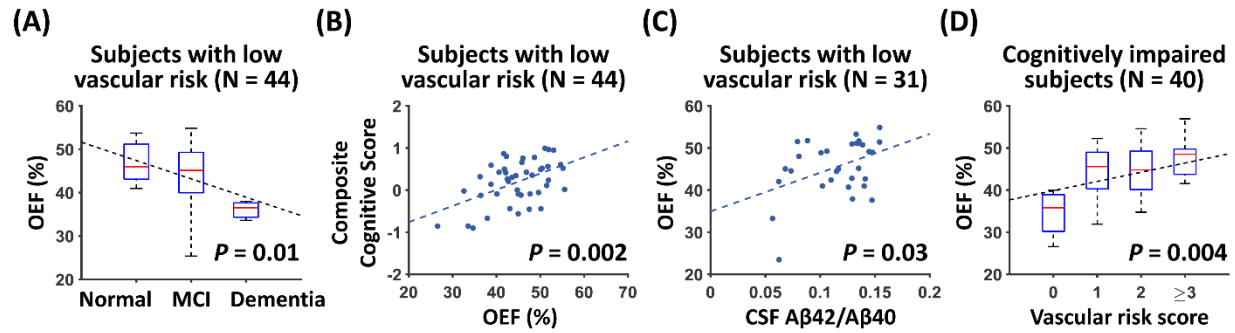


Figure 11. OEF values in elderly individuals, stratified by vascular risk and cognitive diagnosis. In individuals with low vascular risk: (A) patients with mild cognitive impairment (MCI) or dementia had lower OEF; (B) a lower OEF was associated with a worse cognitive performance; and (C) a lower OEF was associated with a lower CSF amyloid-42/amyloid-40 ($A\beta_{42}/A\beta_{40}$) ratio (corresponding to a greater amyloid burden in the brain). (D) In cognitively impaired patients (MCI or dementia), a higher OEF was associated with a greater vascular risk. Adapted from Jiang et al.² with permission.

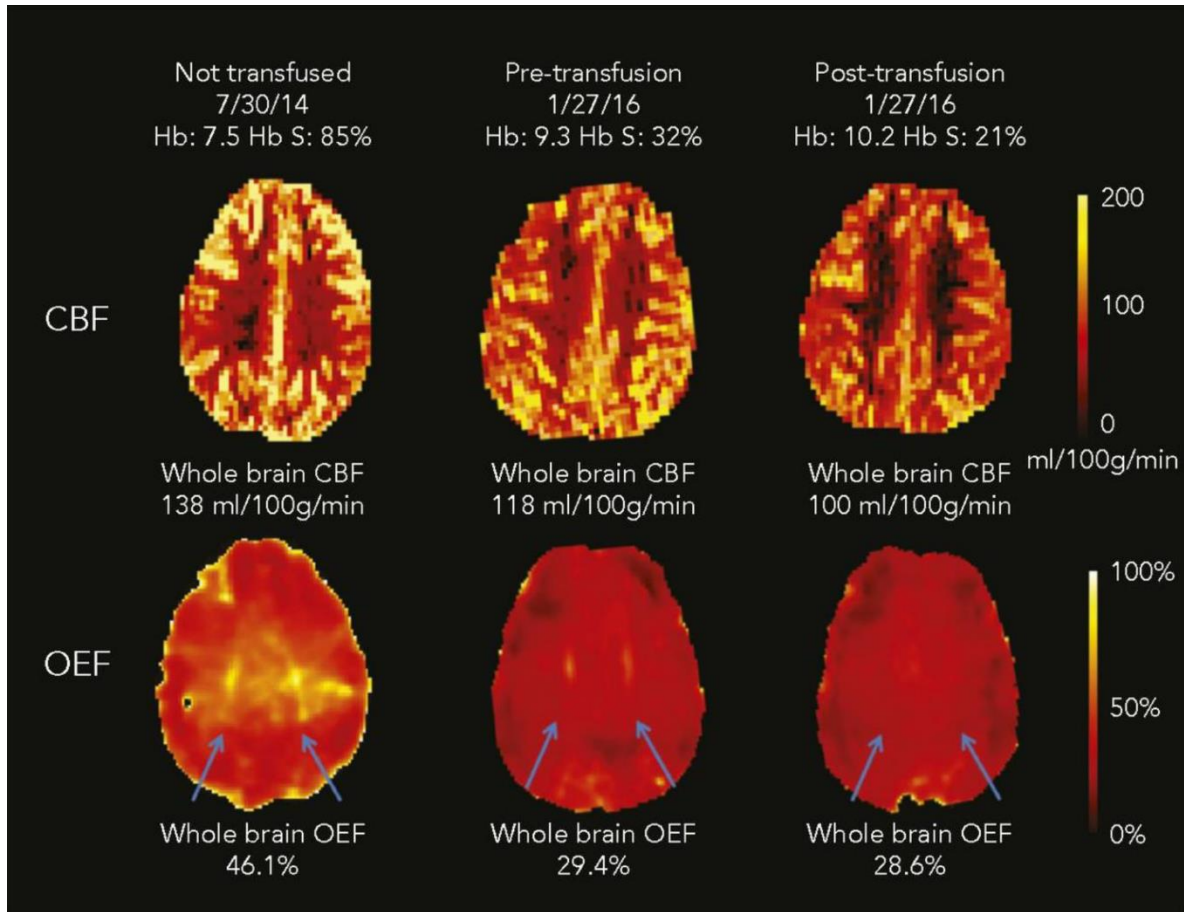


Figure 12. CBF and OEF maps from a child with SCD. This 7-year-old boy underwent an MRI scan before chronic transfusion therapy (CTT) initiation and another two MRI scans before and after an exchange transfusion. The whole-brain CBF was highest at his first scan; after 17 months of CTT, his pretransfusion CBF was lower than the initial scan and the posttransfusion CBF was further decreased. OEF was highest at the first scan, but was dramatically reduced pretransfusion and further decreased posttransfusion. Reproduced from Guilliams et al.²⁵³ with permission.